



Effects of integration time on in-water radiometric profiles

DAVIDE D'ALIMONTE,^{1,2,*} GIUSEPPE ZIBORDI,³ AND TAMITO KAJIYAMA^{1,2}

¹Centro de Investigação Marinha e Ambiental CIMA, Universidade do Algarve, Faro, Portugal

²ÆQUORA Lda, EN 125 Vale Paraíso, Espazo-Box 1105, 8200-567, Albufeira, Portugal

³European Commission, Joint Research Centre, Directorate for Sustainable Resources, Ispra, Italy

*davide.dalimonte@gmail.com

Abstract: This work investigates the effects of integration time on in-water downward irradiance E_d , upward irradiance E_u and upwelling radiance L_u profile data acquired with free-fall hyperspectral systems. Analyzed quantities are the subsurface value and the diffuse attenuation coefficient derived by applying linear and non-linear regression schemes. Case studies include oligotrophic waters (Case-1), as well as waters dominated by colored dissolved organic matter (CDOM) and non-algal particles (NAP). Assuming a 24-bit digitization, measurements resulting from the accumulation of photons over integration times varying between 8 and 2048 ms are evaluated at depths corresponding to: 1) the beginning of each integration interval (FST); 2) the end of each integration interval (LST); 3) the averages of FST and LST values (AVG); and finally 4) the values weighted accounting for the diffuse attenuation coefficient of water (WGT). Statistical figures show that the effects of integration time can bias results well above 5% as a function of the depth definition. Results indicate the validity of the WGT depth definition and the fair applicability of the AVG one. Instead, both the FST and LST depths should not be adopted since they may introduce pronounced biases in E_u and L_u regression products for highly absorbing waters. Finally, the study reconfirms the relevance of combining multiple radiometric casts into a single profile to increase precision of regression products.

© 2018 Optical Society of America under the terms of the [OSA Open Access Publishing Agreement](#)

OCIS codes: (010.5620) Radiative transfer; (010.4450) Oceanic optics; (280.0280) Remote sensing and sensors; (010.5630) Radiometry.

References and links

1. B. A. Franz, S. W. Bailey, P. J. Werdell, and C. R. McClain, "Sensor-independent approach to the vicarious calibration of satellite ocean color radiometry," *Appl. Optics* **46**, 5068–5082 (2007).
2. G. Zibordi, F. Mélin, J.-F. Berthon, and E. Canuti, "Assessment of MERIS ocean color data products for European seas," *Ocean Sci. Discuss.* **9**, 521–533 (2013).
3. T. Kajiyama, D. D'Alimonte, and G. Zibordi, "Match-up analysis of MERIS radiometric data in the Northern Adriatic Sea," *IEEE Geosci. Remote Sens. Lett.* **11**, 19–23 (2014).
4. IOCCG, *Remote Sensing of Ocean Colour in Coastal, and Other Optically-Complex Waters*, S. Sathyendranath, ed. (IOCCG, 2000).
5. D. D'Alimonte, G. Zibordi, T. Kajiyama, and J.-F. Berthon, "Comparison between MERIS and regional high-level products in European seas," *Remote Sens. Environ.* **140**, 378–395 (2014).
6. N. G. Jerlov, *Marine Optics* (Elsevier, 1976).
7. G. Zibordi and K. Voss, *Field Radiometry and Ocean Colour Remote Sensing* (Springer, 2010), Chap. 18.
8. D. K. Clark, M. Feinholz, M. Yarbrough, C. Johnson, Y. S. K. Steven W. Brown, and R. A. Barnes, "Overview of the radiometric calibration of MOBY," *Proc. SPIE* **4483**, 64–76 (2002).
9. D. Antoine, P. Guevel, J.-F. Desté, G. Bécu, F. Louis, A. J. Scott, and P. Bardey, "The "BOUSSOLE" buoy—a new transparent-to-swell taut mooring dedicated to marine optics: Design, tests, and performance at sea," *J. Atmos. Oceanic Tech.* **25**, 968–989 (2008).
10. R. C. Smith, C. R. Booth, and J. L. Star, "Oceanographic biooptical profiling system," *Appl. Optics* **23**, 2791–2797 (1984).
11. G. Zibordi, D. D'Alimonte, and J.-F. Berthon, "An evaluation of depth resolution requirements for optical profiling in coastal waters," *J. Atmos. Oceanic Tech.* **21**, 1059–1073 (2004).

12. D. D'Alimonte and G. Zibordi, "The JRC Data Processing System," in "SeaWiFS Technical Report SERIES" (NASA GSFC, 2001), vol. 15, pp. 52–56.
13. M. Hieronymi and A. Macke, "Spatio-temporal underwater light field fluctuations in the open ocean," *J. Eur. Opt. Soc. Rapid. Publ.* **5**, 10019s (2010).
14. D. D'Alimonte, G. Zibordi, T. Kajiyama, and J. C. Cunha, "Monte Carlo code for high spatial resolution ocean color simulations," *Appl. Optics* **49**, 4936–4950 (2010).
15. M. Hieronymi and A. Macke, "On the influence of wind and waves on underwater irradiance fluctuations," *Ocean Sci.* **8**, 455–471 (2012).
16. M. Hieronymi, A. Macke, and O. Zielinski, "Modeling of wave-induced irradiance variability in the upper ocean mixed layer," *Ocean Sci.* **8**, 103–120 (2012).
17. M. Hieronymi, "Monte Carlo code for the study of the dynamic light field at the wavy atmosphere-ocean interface," *J. Eur. Opt. Soc. Rapid. Publ.* **8**, 13039 (2013).
18. M. Hieronymi, "Polarized reflectance and transmittance distribution functions of the ocean surface," *Opt. Express* **24**, A1045–A1068 (2016).
19. D. D'Alimonte, E. B. Shybanov, G. Zibordi, and T. Kajiyama, "Regression of in-water radiometric profile data," *Opt. Express* **21**, 27707–27733 (2013).
20. T. Kajiyama, D. D'Alimonte, J. C. Cunha, and G. Zibordi, "High-performance ocean color Monte Carlo simulation in the Geo-info project," in *Parallel Processing and Applied Mathematics, Lecture Notes in Computer Science*, R. Wyrzykowski, J. Dongarra, K. Karczewski, and J. Wasniewski, eds. (Springer, 2010), vol. 6068, pp. 370–379.
21. T. Kajiyama, D. D'Alimonte, and J. C. Cunha, "Performance prediction of ocean color Monte Carlo simulations using multi-layer perceptron neural networks," in *Procedia Computer Science*, M. Sato, S. Matsuoka, P. M. Slood, G. D. van Albada, and J. Dongarra, eds. (Elsevier, 2011), vol. 4, pp. 2186–2195.
22. B. Bulgarelli and D. D'Alimonte, "Simulation of in situ visible radiometric measurements," in *Optical Radiometry for Oceans Climate Measurements*, G. Zibordi, C. Donlon, and A. Parr, eds. (Elsevier, 2014), Chap. 3.
23. D. D'Alimonte and T. Kajiyama, "Effects of light polarization and waves slope statistics on the sea-surface reflectance," *Opt. Express* **24**, 7922–7942 (2016).
24. T. Kajiyama, D. D'Alimonte, and J. C. Cunha, "A high-performance computing framework for Monte Carlo ocean color simulations," *Concurrency Computat.: Pract. Exper.* **29**, e3860 (2017).
25. V. V. Sobolev, *Light Scattering in Planetary Atmospheres* (Pergamon, 1975).
26. R. Penndorf, "Tables of the refractive index for standard air and the Rayleigh scattering coefficient for the spectral region between 0.2 and 20.0 μ and their application to atmospheric optics," *J. Opt. Soc. Am.* **47**, 176–182 (1957).
27. J. E. Hansen and L. D. Travis, "Light scattering in planetary atmospheres," *Space Sci. Rev.* **16**, 527–610 (1974).
28. H. C. Van De Hulst, *Light Scattering by Small Particles* (Dover Publications, 1957).
29. S. Chandrasekhar, *Radiative Transfer* (Dover Publications, 1960).
30. C. F. Bohren and D. R. Huffman, *Absorption and Scattering of Light by Small Particles* (John Wiley and Sons, 1983).
31. C. Emde, R. Buras, B. Mayer, and M. Blumthaler, "The impact of aerosols on polarized sky radiance: model development, validation, and applications," *Atmos. Chem. Phys. Discuss.* **9**, 17753–17791 (2009).
32. C. D. Mobley, "Polarized reflectance and transmittance properties of windblown sea surfaces," *Appl. Opt.* **54**, 4828–4849 (2015).
33. T. Elfouhaily, B. Chapron, K. Katsaros, and D. Vandemark, "A unified directional spectrum for long and short wind-driven waves," *J. Geophys. Res. Oc.* **102** 15781–15796 (1997).
34. G. R. Fournier and J. L. Forand, "Analytic phase function for ocean water," *Proc. SPIE* **4483**, 194–201 (1994).
35. G. R. Fournier and M. Jonasz, "Computer-based Underwater Imaging Analysis," *Proc. SPIE* **3761**, 62–70 (1999).
36. J. R. V. Zaneveld, E. Boss, and A. Barnard, "Influence of surface waves on measured and modeled irradiance profiles," *Appl. Optics* **40**, 1442–1449 (2001).
37. J. Escher and T. Schlurmann, "On the recovery of the free surface from the pressure within periodic traveling water waves," *J. Nonlinear Math. Phys.* **15**, 50–57 (2008).
38. N. L. Jones and S. G. Monismith, "Measuring short-period wind waves in a tidally forced environment with a subsurface pressure gauge," *Limnol. Oceanogr.: Methods* **5**, 317–327 (2007).
39. C. Tsai, M. Huang, F. Young, Y. Lin, and H. Li, "On the recovery of surface wave by pressure transfer function," *Ocean Eng.* **32**, 1247–1259 (2005).
40. P. J. Werdell and S. W. Bailey, "An improved in-situ bio-optical data set for ocean color algorithm development and satellite data product validation," *Remote Sens. Environ.* **98**, 122–140 (2005).
41. G. Zibordi, J.-F. Berthon, F. Mélin, and D. D'Alimonte, "Cross-site consistent in situ measurements for satellite ocean color applications: the BiOMaP radiometric dataset," *Remote Sens. Environ.* **115**, 2104–2115 (2011).
42. D. Schattschneider, "Proof without words: The arithmetic mean-geometric mean inequality," *Math. Mag.* **59**, 11 (1986).
43. J. L. Mueller and R. W. Austin, "Ocean Optics Protocols SeaWiFS for Validation, Revision 1," in "SeaWiFS Technical Report SERIES" (NASA GSFC, 1995) vol. 25, pp. 48–59.
44. S. Hooker, G. Zibordi, J.-F. Berthon, D. D'Alimonte, S. Maritorena, S. Mclean, and J. Sildam, "Results of the Second SeaWiFS Data Analysis Round Robin," in "SeaWiFS Technical Report SERIES" (NASA GSFC, 2001), vol. 15, pp. 4–45.
45. Y. You, D. Stramski, M. Darecki, and G. W. Kattawar, "Modeling of wave-induced irradiance fluctuations at

- near-surface depths in the ocean: a comparison with measurements,” *Appl. Optics* **49**, 1041–1053 (2010).
46. D. A. Siegel, “Results of the SeaWiFS Data Analysis Round-Robin,” in “SeaWiFS Technical Report SERIES” (NASA GSFC, 1995), vol. 26, pp. 44–48.
47. G. A. F. Seber and C. J. Wild, *Nonlinear Regression* (J. Wiley & Sons, 2003).
48. Y. Yuan, “A Review of Trust Region Algorithms for Optimization,” in “Proceedings of the Fourth International Congress on Industrial and Applied Mathematics”, J. M. Ball, and J. C. R. Hunt, eds. (Oxford University Press, 2000), pp. 271–282.
49. M. H. DeGroot and M. J. Schervish, *Probability and Statistics* (Addison Wesley, 2012).

1. Introduction

The collection of field measurements with in-water optical systems underpins a number of ocean color applications including the assessment and vicarious calibration of space-borne radiometric data [1–3], or the development of inversion schemes to obtain maps of derived products [4, 5]. Following early developments [6], in-water radiometers can be roughly separated into fixed-depth and profiling systems [7]. Fixed-depth radiometers are generally operated on bio-optical buoys [8, 9]. In-water radiometric profiling is instead performed through winched or free-fall systems. Winched systems were extensively used for many years and are still applied on specific deployment platforms [10, 11]. Free-fall systems introduced during the late 1980s, have been increasingly used to perform measurements from ships during oceanographic campaigns [7, 11, 12].

Uncertainty requirements for in situ radiometric measurements are strictly connected to the specific application [7]. For instance, the validation of satellite radiometric products such as the water-leaving radiance determined from at-the-satellite radiance corrected for atmospheric perturbations, implies the use of in situ data affected by uncertainties generally below 5% across the visible spectrum. These uncertainties should be even lower for in situ data applied for the indirect calibration of space sensors (*i.e.*, system vicarious calibration).

A comprehensive quantification of the uncertainties affecting in situ measurements implies accounting for contributions due to calibration, sensors performance (*e.g.*, linearity and temperature responses), effects of environmental variability (*e.g.*, light focusing and defocusing by wave facets), data reduction algorithms (*e.g.*, extrapolation of sub-surface values), and perturbations by instrument housing and deployment platform (*e.g.*, shading). It is also important that each of these contributions is kept to within small values, ideally not exceeding 1–2% to avoid that combined uncertainties may pass the target thresholds.

Within such a general context, the scope of the present study is to investigate the effects of integration time on optical data from in-water profiling systems. Analyzed quantities are the downward irradiance E_d , the upward irradiance E_u and the upwelling radiance L_u , henceforth generically denoted \mathfrak{R} . Considered data products are the subsurface value \mathfrak{R}_0 and the diffuse attenuation coefficient $K_{\mathfrak{R}}$, derived from the regression of radiometric measurements acquired at different depths (negative downwards in this study) and hereafter indicated as regression products. The sampling setting is defined by a constant deployment speed v_{prf} and a dynamical integration time t that increases at the lessening of the radiometric signal. Specifically, the in-water i -th optical measurement is obtained through the accumulation of photons collected within a depth increment $\Delta_z = -v_{\text{prf}} \cdot t$. The recorded value denoted with the tilde notation is

$$\tilde{\mathfrak{R}}(z_i^*) = \frac{1}{\Delta_z} \int_{z_i}^{z_i + \Delta_z} \mathfrak{R}(z') dz', \quad (1)$$

where the sampling depth $z_i^* \in [z_i, z_i + \Delta_z]$ has to be determined so that a difference between the measured $\tilde{\mathfrak{R}}(z_i^*)$ and the actual $\mathfrak{R}(z_i^*)$ radiometric value is minimized and consequently does not affect the determination of \mathfrak{R}_0 and $K_{\mathfrak{R}}$. This requirement is addressed in the present study accounting that \mathfrak{R} is a non-linear function of z .

The effects of integration time can be individually studied in the ideal condition of a still sea. In real cases, environmental factors and data reduction solutions combine with the uncertainties affecting \mathfrak{K}_0 and $K_{\mathfrak{K}}$. For instance, wind-driven waves at the air-water interface, besides focusing and defocusing the light [13–18], can influence the response of the pressure gauge at the depth of the optical system. Linear and non-linear data reduction schemes can also lead to slightly different results [19]. Overall, the effects of integration time, which convolve with uncertainties from environmental perturbations and processing solutions, affect the various radiometric quantities.

All these elements are considered in the present study to stress measurement and processing solutions in view of increasing the quality of in situ radiometric data products from hyperspectral in-water free-fall profiles. The study is executed using the MOX Monte Carlo code to simulate radiometric fields for different measurement conditions by applying high-performance computing solutions [14, 19–24]. The response of in-water optical sensors is investigated based on a two-dimensional representation of the underwater light distribution.

Study results are obtained assuming an ideal hyperspectral radiometer with negligible delays (*i.e.*, null latency time) between the end of a measurement and the start of the successive one, signal digitization through a 24-bit analog-to-digital converter (ADC) and an overall uncertainty of 10 counts. Actual measurements are then discussed by: 1) addressing wavelength-specific integration times; 2) accounting for 16-bit digitization and non-negligible latency time; and 3) evaluating the effects of an increase of the radiometric measurements per unit depth adopting the multicasting scheme.

2. Data and methods

This section presents the methods applied to: 1) model the sky-radiance distribution; 2) represent the air-sea interface as a function of the wind speed v_{wnd} ; 3) generate the in-water radiometric field; 4) produce virtual radiometric profiles accounting for the effects of integration time; and 5) compute regression products using linear LN and non-linear NL reduction schemes.

The radiance distribution of a clear sky is largely determined by the sun zenith and the optical properties of the atmospheric constituents (mostly aerosols and air molecules). Similarly, the in-water light distribution depends on the seawater Inherent Optical Properties (IOPs) and, on a lesser extent, on sea-surface waves. To minimize computing time, in this work the sky- and in-water radiance distributions are modeled separately. This allows for applying the same sky dome to initialize the photon tracing in a number of in-water radiometric simulations with different IOPs and/or sea-surface configurations.

Table 1. Parameters for Simulating the Sky-radiance Distribution at $\lambda = 490$ nm.

| Parameter | Symbol | Value | Units |
|---|-----------------------|------------------------|-----------------|
| Sun zenith | θ_{sun} | 30° | deg. |
| Atmosphere top | h_{atm} | 10 ⁴ | m |
| Bottom reflectance (Lambertian) | R_b | 5 | % |
| Scattering optical thickness of molecules | τ_b^M | 0.1584 | |
| Scattering optical thickness of aerosol | τ_b^A | 0.23 | |
| Total scattering optical thickness | τ_b | 0.3884 | |
| Absorption optical thickness of ozone | τ_a^O | 0.00632 | |
| Total absorption optical thickness | τ_a | 0.00632 | |
| Absorption | a_{atm} | $0.0630 \cdot 10^{-5}$ | m ⁻¹ |
| Scattering | b_{atm} | $3.8842 \cdot 10^{-5}$ | m ⁻¹ |
| Attenuation | c_{atm} | $3.9472 \cdot 10^{-5}$ | m ⁻¹ |
| Single scattering albedo | ω_{atm} | 0.9840 | |
| Photon population | N_{ph} | 10 ⁹ | |

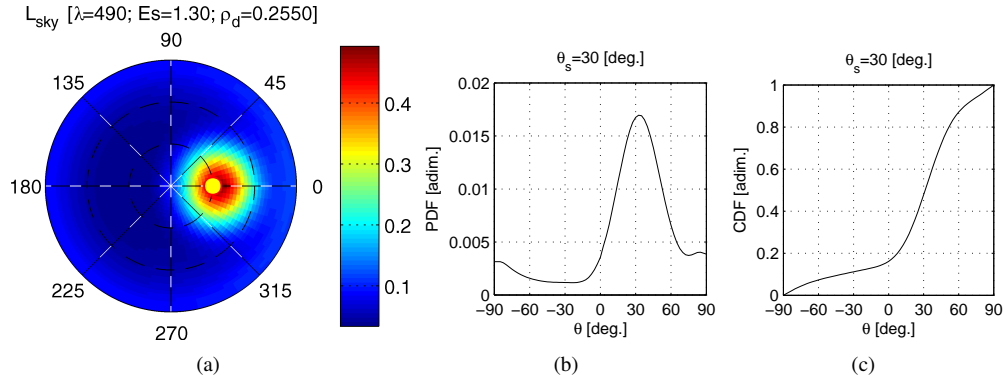


Fig. 1. Panel (a) shows an example of the distribution of the diffuse sky-radiance (*i.e.*, without the solar disk) for $\theta_{\text{sun}} = 30^\circ$ and in units of $\text{W m}^{-2} \text{nm}^{-1}$. The probability density function (PDF) and the cumulative distribution function (CDF) of incoming photon direction θ in the solar plane are presented in panels (b) and (c), respectively.

2.1. Sky-radiance distribution

In addition to the overcast illumination case, the diffuse sky radiance is defined for a sun zenith θ_{sun} of 30° [see Fig. 1 and Table 1] in plane-parallel, homogeneous and cloud-free conditions [25] with ideal Lambertian bottom. The photons tracing is at first performed in the atmospheric domain. The cumulative distribution function (CDF) for initializing the photon direction above the sea-surface is then derived from the solar plane of the full sky dome. The diffuse-to-total ratio ρ_d between diffuse and total irradiance is also evaluated (Table 2 [23]).

Atmospheric optical properties are specified at $\lambda = 490$ nm chosen as representative wavelength for this analysis. The scattering optical thickness of the atmosphere is $\tau_b = \tau_b^M + \tau_b^A$, where τ_b^M and τ_b^A denote the molecules M and aerosol A contributions, respectively. The absorption optical thickness is instead $\tau_a = \tau_a^O + \tau_a^G$, with τ_a^O and τ_a^G accounting for weak contributions of ozone O and permanent gases G, respectively. The absorption a_{atm} and scattering b_{atm} coefficients are defined scaling the optical thickness by the atmosphere height, and assuming that the scattering rather than absorption determines the aerosol contribution.

The Monte Carlo path length l of the photon trajectory in the atmosphere is

$$l = -\log(u)/c_{\text{atm}} \quad (2)$$

where $c_{\text{atm}} = a_{\text{atm}} + b_{\text{atm}}$ is the attenuation coefficient and u is a random number sampled from a uniform distribution between 0 and 1; *i.e.*, $u \in \mathcal{U}(0, 1)$.

The photon weight is updated as

$$w_{\text{new}} = w_{\text{old}} \cdot \omega_{\text{atm}}, \quad (3)$$

where $\omega_{\text{atm}} = b_{\text{atm}}/c_{\text{atm}}$ is the single scattering albedo.

Table 2. Parameters Determining the Overcast and Clear Sky Illumination Conditions.

| Illumination Conditions | θ_{sun} [deg.] | Diffuse over Total |
|-------------------------|------------------------------|--------------------|
| Overcast | NA | 1 |
| Clear sky | 30 | 0.256 |

Table 3. Examples of Sea-surface Statistical Figures.

| Surface Perturbations | Wind Speed [ms ⁻¹] | Elevation Variance [m ²] | | Slope variance [-] | |
|-----------------------|--------------------------------|--------------------------------------|------------------|--------------------|------------------|
| | | Expected Values | Computed Results | Expected Values | Computed Results |
| None | 0 | 0 | 0 | 0 | 0 |
| Medium | 4 | 0.00537 | 0.00527 | 0.02550 | 0.02562 |
| High | 8 | 0.08822 | 0.10448 | 0.04671 | 0.04727 |

Photons ending their trajectory in the atmosphere undergo Rayleigh scattering by air-molecules if $u < \mu$, where $u \in \mathcal{U}(0, 1)$ and $\mu = \tau_b^M / \tau_b$ [26, 27]. The Mie theory defines the aerosol scattering when $u \geq \mu$ [27–31].

2.2. Sea surface modeling

The sea surface is defined over a domain of 40m length discretized by $N_s = 32768$ points (2^{15}), which leads to a resolution of $\Delta_s = L_x / N_s = 1.2$ mm and spatial coordinate $x(s) = s \cdot \Delta_s$ with $s = 1, \dots, N_s$. The sea-surface elevation $z(s)$ is expressed under the assumption of linear wave theory applying the Inverse Fast Fourier Transform (IFFT, [32])

$$z(s) = \frac{1}{N_u} \sum_{u=1}^{N_u} \hat{z}(u) e^{i(s \cdot u / N_u)}, \quad (4)$$

where the harmonic components $\hat{z}(u)$ are indexed in the wavenumber k domain. The $\hat{z}(u)$ values are set based on the Elfouhaily omnidirectional spectral density $\mathcal{S}(k)$ [32, 33], which determines the variance of the sea-surface elevation as a function of the wind speed v_{wnd} and additionally of the wave age.

A fully developed sea is modeled in this study by: 1) computing the two-sided discrete values of the elevation variance; 2) sampling the amplitudes of the harmonic components with normal distributions; and 3) defining the IFFT Hermitian coefficients to obtain a real-valued $z(s)$. The spectral density function $\mathcal{S}(k)$ is iteratively adjusted until converging to the target value [23]. Statistical figures of wind-induced surface perturbations are summarized in Table 3 for v_{wnd} values of 4 and 8 ms⁻¹.

2.3. In-water radiometric simulations

Ray tracing starts at a random point above the sea surface determined by the photon cosine directors μ_x and μ_z , as well as the photon weight w . The photon source is either the sun (direct light) or the sky (diffuse light) quantified in Table 2 as a function of the diffuse-to-total ratio ρ_d of the downward irradiance. If the photon comes from the sun, the initial travel direction is given by the sun zenith angle θ_{sun} and its weight is the unity. Otherwise, the cumulative distribution function derived from the sky radiance is used to initialize the photon direction and weight [see Fig. 1(c)]. The Snell and Fresnel equations redefine the photon properties across the sea-surface.

Table 4. Settings of In-water Radiometric Simulations.

| Parameter | Symbol | Input Value(s) | Units |
|-------------------------|-----------------|----------------------------|-------|
| Domain width | L_x | 40 | m |
| Domain depth | z_b | -20 and -50 | m |
| Domain x-resolution | Δx | 0.01 | m |
| Domain z-resolution | Δz | 0.001 | m |
| Photon population | N_{ph} | [up to $2 \cdot 10^{10}$] | |
| Photon weight threshold | ζ_w | 10^{-6} | |

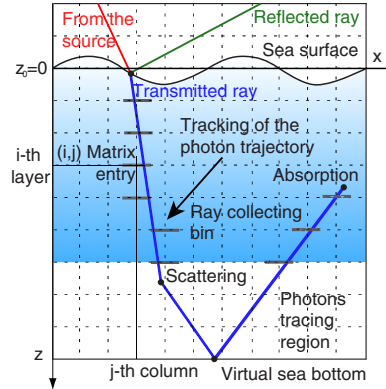


Fig. 2. Schematics of photon tracing. The radiometric sensor of the virtual profiler is represented by the “ray collecting bins” located at the nodes of the simulation grid.

In-water radiometric fields are simulated in a domain with horizontal 0.01 m and vertical 0.001 m resolution (Fig. 2 and Table 4). The in-water free path length traveled by a photon before absorption or scattering follows the exponential probability density function $p(\tau) = \exp(-\tau)$, where $\tau = c \cdot r$ is the optical distance, c is the attenuation coefficient of seawater [m^{-1}], and r [m] is the geometric distance. The Monte Carlo photon tracing is executed solving $P(\tau) = u$ for τ , where P is the cumulative distribution function of the optical distance and $u \in \mathcal{U}(0, 1)$.

The photon weight is scaled at the end of each free path by the single scattering albedo $\omega = (c - a)/c$, where a is the absorption coefficient of seawater [m^{-1}]. The new direction is obtained from the volume scattering function $\beta(\theta)$ [$\text{m}^{-1} \text{sr}^{-1}$]. Namely, the scattering coefficient $b = c - a$ and scattering phase function $\tilde{\beta} = \beta/b$ define the probability density function $p(\theta) = 2\pi\tilde{\beta}(\theta) \sin(\theta)$. Each zenith angle of scattering θ is sampled by solving $P(\theta) = u$ for θ , where P is the cumulative distribution function of the scattering angle θ and $u \in \mathcal{U}(0, 1)$. The azimuth scattering angle is randomly chosen between 0 and 2π . If a photon hits the left (right) side of the domain, its trajectory is continued from the right (left) side at the same depth thanks to the periodicity of sea-surface waves.

A photon that reaches the lower boundary of the simulation domain is upward scattered with its weight scaled by the irradiance reflectance factor $R_b = E_u/E_d$. The bottom depths z_b and the related reflectances reported in Table 5 have been pre-determined for each water type by performing a preliminary set of low-resolution simulations in a water column of 100m neglecting the bottom effects (details not presented). This solution, which attempts to approximate an infinitely deep sea, has been implemented to meet computational constraints.

The new cosine directors of photons scattered by the virtual bottom are $\mu_z = \sqrt{u}$ and $\mu_x = \sqrt{1 - \mu_z^2} \cdot \text{sign}(q - 0.5)$, where q and u are independent random numbers in $\mathcal{U}(0, 1)$ and $\text{sign}(x) = x/|x|$. The photon tracing ends when its weight becomes lower than the threshold $\zeta_w = 10^{-6}$.

Each time a photon intersects a ray-collecting-bin representing the detector [see Fig. 2], its weight is added to the corresponding entry of matrices expressing the radiometric fields according to the following rules: 1) $\mu_z < 0$ for E_d ; 2) $\mu_z > 0$ for E_u ; and 3) $\mu_z > \cos(\text{FAFOV}/2)$ for L_u , where the full-angle field of view (FAFOV) for radiance measurements is set to 20° . Photons are traced within the entire water column, but their contribution to radiometric fields (tracking of the ray trajectory) is taken into account only between 0 and -10m to meet computing time and

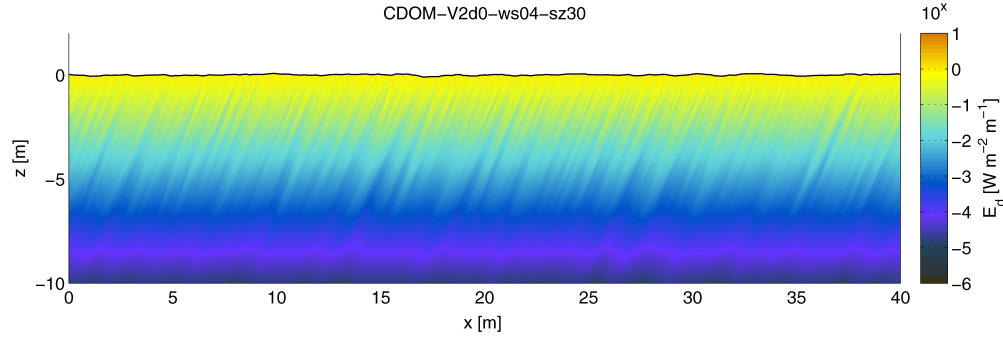


Fig. 3. Example of an E_d radiometric field simulated for highly absorbing marine waters (CDOM-dominated), $v_{\text{wnd}} = 4 \text{ ms}^{-1}$ and $\theta_{\text{sun}} = 30^\circ$.

memory requirements.

The response of in-water optical sensors is analyzed in the following cases:

1. oligotrophic waters (Case-1).
2. waters characterized by high concentration of Colored Dissolved Organic Matter (CDOM-dominated).
3. waters characterized by high concentration of Non-Algal Particles (NAP-dominated).

Table 5 reports the corresponding IOP values whereas Fig. 3 shows an example of E_d simulations.

2.3.1. Virtual profiling

In the reality, waves travel at the surface while the radiometric sensors descend vertically to generate the optical profile. To optimize simulation efficiency, the present study considers a diagonal virtual profile below a static sea surface as illustrated in Fig. 4 [14, 19, 36]. Differences between the phase velocities of sea-surface waves are neglected assuming that all translate at the same v_{wav} speed

$$v_{\text{wav}} = \sqrt{\frac{g \cdot l_{\text{wav}}}{2\pi}}, \quad (5)$$

where $l_{\text{wav}} = 20\text{m}$ is the longest wave that the IFFT can represent in the simulation domain (Eq. (4); [23, 32]) and g is the acceleration due to gravity. The angle of the virtual profile θ_{prf} with respect to zenith is then

$$\theta_{\text{prf}} = \arctg \frac{v_{\text{wav}}}{v_{\text{prf}}} \quad (6)$$

Table 5. Inherent Optical Properties (Absorption a , Attenuation c and Single Scattering Albedo ω) as well as Properties of the Virtual Bottom (Depth z_b and Reflectance Value R_b) Adopted to Perform Monte Carlo Simulations for Different Marine Optical Cases. The Coefficients of the Fournier-Forand Volume Scattering Function [34, 35] are: Slope of the Junge Distribution $m = 3.5835$ and Refraction Index $n = 1.1$.

| Water Type | a [m^{-1}] | c [m^{-1}] | ω | Bottom | |
|------------|----------------------------|----------------------------|----------|-----------|-----------------|
| | | | | z_b [m] | $R_b = E_u/E_d$ |
| Case-1 | 0.01 | 0.10 | 0.90 | -50 | 0.062 |
| CDOM | 1.20 | 1.00 | 0.17 | -20 | 0.001 |
| NAP | 0.20 | 1.00 | 0.80 | -20 | 0.030 |

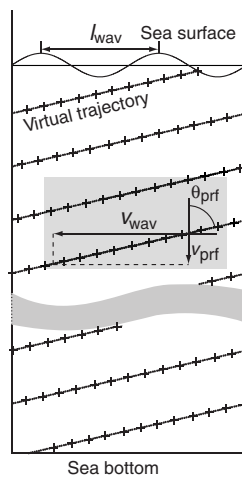


Fig. 4. Example of diagonal virtual trajectory below a fixed sea surface applied to compute the optical profile (see text for details).

with v_{prf} values between 0.2 and 1.0ms^{-1} .

2.3.2. Pressure gauge correction

The still level $z_0=0$, at which radiometric data products are ideally referred to, can differ from the depth sensed by a pressure gauge under a wavy sea-surface $z_s(x)$. This effect is considered applying a pressure transfer model derived from the linear wave theory [37–39]. The adjusted depth $z_g(x)$ of a photon collecting bin located at the grid-depth z (*i.e.*, the actual distance from z_0) is computed as

$$z_g(x) = z + e^{z \cdot k_{wav}} z_s(x), \tag{7}$$

where $k_{wav} = 2\pi/l_{wav}$ denotes the wave number, l_{wav} is set to 20m as in Eq. (5), and the water column is assumed infinitely deep. Fig. 5 shows how the effect of the pressure gauge correction varies with depth.

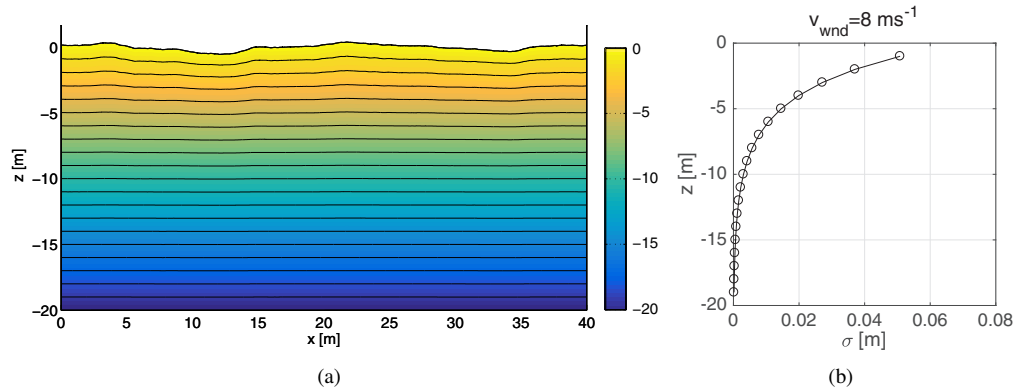


Fig. 5. (a) Example of iso-depth lines accounting for the pressure gauge correction due to surface waves generated with $v_{wnd} = 8\text{ms}^{-1}$. (b) Standard deviation of the difference between subsequent iso-depth lines.

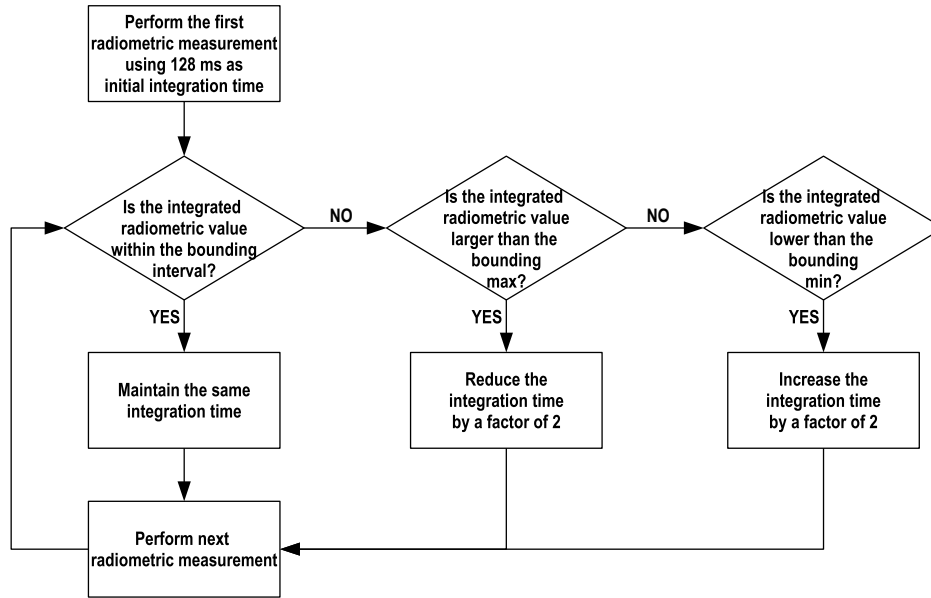


Fig. 6. Schematic of the process determining the integration times applied for measuring E_d , E_u and L_u values. The radiometric boundaries are specified in Table 6.

2.3.3. Integrated radiometric values and measurement depth definition

In situ radiometric measurements are simulated by relying on the schematic of Fig. 6, and the integration times with the related radiometric intervals listed in Table 6. The Min and Max radiometric values were determined accounting for 15% and 80% of the digitization range, respectively. Noise was added to the digitized signal by sampling from a normal distribution with standard deviation of 10 counts regardless of the integration time.

Alternative measurement depths are considered for each radiometric value resulting from the accumulation of photons (integration) over time intervals between 8 and 2048 ms. These include:

- 1) the depths corresponding to the beginning of each integration interval (FST);
- 2) those corresponding to the end of each integration interval (LST);
- 3) the averages of FST and LST values (AVG); and finally
- 4) the values weighted accounting for the diffuse attenuation coefficient of water determined for each radiometric quantity (WGT).

The WGT method assumes an exponential decay of the radiometric quantity $\mathfrak{R}(z) = \mathfrak{R}_0 \cdot e^{K_{\mathfrak{R}} \cdot z}$, where $K_{\mathfrak{R}} > 0$, z is negative downward and \mathfrak{R}_0 is set to 1 without loss of generality (Fig. 7). The integrated value $\tilde{\mathfrak{R}}_{z_i}^{z_i + \Delta_z}$ between z_i and $z_i + \Delta_z$ (for $\Delta_z < 0$) is

$$\tilde{\mathfrak{R}}_{z_i}^{z_i + \Delta_z} = \frac{1}{\Delta_z} \int_{z_i}^{z_i + \Delta_z} e^{K_{\mathfrak{R}} \cdot z} dz = \frac{e^{K_{\mathfrak{R}} \cdot (z_i + \Delta_z)} - e^{K_{\mathfrak{R}} \cdot z_i}}{K_{\mathfrak{R}} \cdot \Delta_z}, \quad (8)$$

and there is a z_i^* depth between z_i and $z_i + \Delta_z$ such that

$$e^{K_{\mathfrak{R}} \cdot z_i^*} = \frac{e^{K_{\mathfrak{R}} \cdot (z_i + \Delta_z)} - e^{K_{\mathfrak{R}} \cdot z_i}}{K_{\mathfrak{R}} \cdot \Delta_z}, \quad (9)$$

Table 6. Values of the Integration Time for E_d and L_u [see also Fig. 6]. The Intervals for E_u are the Same as for E_d . These Intervals were Determined to Mimic those Actually Implemented in HyperOCR Radiometers Manufactured by Satlantic (Halifax, NS, Canada).

| Index i | Integration time $T(i)$ [ms] | Boundaries $B(i)$ | | | |
|-----------|------------------------------|------------------------------|----------|--------------------------------------|----------|
| | | E_d [$W m^{-2} nm^{-1}$] | | L_u [$W m^{-2} nm^{-1} sr^{-1}$] | |
| | | Max | Min | Max | Min |
| 1 | 8 [2^3] | 17.871902 | 3.973027 | 0.816625 | 0.181826 |
| 2 | 16 [2^4] | 8.935951 | 1.986514 | 0.408313 | 0.090913 |
| 3 | 32 [2^5] | 4.467975 | 0.993257 | 0.204156 | 0.045456 |
| 4 | 64 [2^6] | 2.233988 | 0.496628 | 0.102078 | 0.022728 |
| 5 | 128 [2^7] | 1.116994 | 0.248314 | 0.051039 | 0.011364 |
| 6 | 256 [2^8] | 0.558497 | 0.124157 | 0.025520 | 0.005682 |
| 7 | 512 [2^9] | 0.279248 | 0.062079 | 0.012760 | 0.002841 |
| 8 | 1024 [2^{10}] | 0.139624 | 0.031039 | 0.006380 | 0.001421 |
| 9 | 2048 [2^{11}] | 0.069812 | 0.015520 | 0.003190 | 0.000710 |

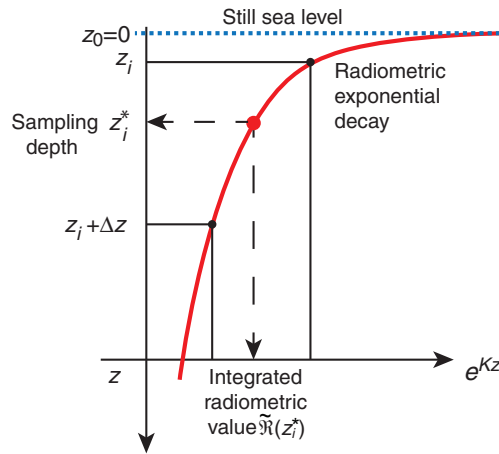


Fig. 7. Schematics of the weighted (WGR) measurement depth determined as a function of the diffuse attenuation coefficient.

which solved for z_i^* leads to

$$z_i^* = \frac{1}{K_{\mathfrak{R}}} \ln \left(\tilde{\mathfrak{R}}_{z_i + \Delta z} \right). \tag{10}$$

In summary, the WGR method associates the depth z_i^* to the integrated radiometric value $\tilde{\mathfrak{R}}_{z_i + \Delta z}$.

2.3.4. Data reduction schemes

Linear and non-linear regression schemes [19] are both considered for the determination of radiometric regression products. The rationale is to determine differences between the two methods accounting for the convoluted effects of the integration time with other perturbing factors such as the light focusing and the pressure gauge response below a wavy sea surface.

The linear regression The classical solution to determine \mathfrak{R}_0 and $K_{\mathfrak{R}}$ is based on the linear regression (LN) as a function of z of the log-transformed $\mathfrak{R}(z)$ values [7, 40, 41]. The underlying

assumption is the exponential decay

$$\mathfrak{R}(z) = \mathfrak{R}_0 e^{K_{\mathfrak{R}} \cdot z} \quad (11)$$

in a water layer where $K_{\mathfrak{R}}$ is constant (it is remarked that different from common conventions, depth values are negative in this work). In the logarithmic form, Eq. (11) becomes

$$\log(\mathfrak{R}(z)) = \log(\mathfrak{R}_0) + K_{\mathfrak{R}} \cdot z. \quad (12)$$

The LN method utilizes Eq. (12) to determine regression parameters by minimizing the sum-of-squares SSE error

$$\text{SSE}^{\text{LN}}(\mathfrak{R}_0, K_{\mathfrak{R}}) = \sum_{i=1}^N \left\{ \log[\tilde{\mathfrak{R}}(z_i^*)] - [\log(\mathfrak{R}_0) + K_{\mathfrak{R}} \cdot z_i^*] \right\}^2, \quad (13)$$

which is solved as a linear system of equations.

The non-linear regression The average of log-transformed values is equal or lower than the logarithm of their averages because of the inequality between the arithmetic and the geometric mean [19, 42]. This can bias linear regression results. Offset corrections are difficult since perturbations due to light focusing and defocusing largely vary in the water column [11, 15, 16, 36, 43–46]. The nonlinear NL approach [47] has been proposed to compute \mathfrak{R}_0 and $K_{\mathfrak{R}}$ by minimizing the SSE^{NL} error function

$$\text{SSE}^{\text{NL}}(\mathfrak{R}_0, K_{\mathfrak{R}}) = \sum_{i=1}^N [\tilde{\mathfrak{R}}(z_i^*) - \mathfrak{R}_0 e^{K_{\mathfrak{R}} \cdot z_i^*}]^2 \quad (14)$$

without taking the logarithm of $\tilde{\mathfrak{R}}(z_i^*)$ values. The partial derivatives of Eq. (14) however lead to a non-linear system and the Trust-Region algorithm [47, 48] is applied in this work to minimize SSE^{NL} . A set of trials based on the re-initialization of the Trust-Region scheme are also executed to verify the convergence of the NL solution.

3. Results

3.1. Statistical figures

The depth separation between the data points of the FULL resolution virtual profile is about the same as the vertical grid spacing of the simulation domain (*i.e.*, 0.001 m; see Table 4). The corresponding NL data products are denoted as $\{[\mathfrak{Y}]_{\text{FULL}}^{\text{NL}}\}^{\text{S}}$, where \mathfrak{Y} indicates the \mathfrak{R}_0 or $K_{\mathfrak{R}}$ regression products, and S denotes the environmental case (*i.e.*, water type, illumination condition, wind speed) and the measurement setting (*i.e.*, sensor deployment speed). The $\{[\mathfrak{Y}]_{\text{FULL}}^{\text{NL}}\}^{\text{S}}$ values, not affected by the integration time nor biased by the log-transformation (Sec. 2.3.4), represent the reference quantities for this study. Alternative regression results compared with $\{[\mathfrak{Y}]_{\text{FULL}}^{\text{NL}}\}^{\text{S}}$, instead, depend on the sampling depth definition (Sec. 2.3.3) and the data reduction scheme (LN or NL, Sec. 2.3.4). As an example, $\{[\mathfrak{Y}]_{\text{FST}}^{\text{LN}}\}^{\text{S}}$ indicates the LN regression of integrated radiometric data adopting the FST depth definition. The percent difference $\{[\delta_{\mathfrak{Y}}]_{\text{FST}}^{\text{LN}}\}^{\text{S}}$ between $\{[\mathfrak{Y}]_{\text{FST}}^{\text{LN}}\}^{\text{S}}$ and $\{[\mathfrak{Y}]_{\text{FULL}}^{\text{NL}}\}^{\text{S}}$ is computed as

$$\{[\delta_{\mathfrak{Y}}]_{\text{FST}}^{\text{LN}}\}^{\text{S}} = 100 \cdot \frac{1}{N} \sum_{n=1}^N \frac{\{[\mathfrak{Y}]_{\text{FST}}^{\text{LN}}\}_n^{\text{S}} - \{[\mathfrak{Y}]_{\text{FULL}}^{\text{NL}}\}_n^{\text{S}}}{\{[\mathfrak{Y}]_{\text{FULL}}^{\text{NL}}\}_n^{\text{S}}}, \quad (15)$$

Table 7. List of Symbols of the Data Products Analyzed in this Study.

| Topic | Symbol | Description |
|-------------------|--------|--|
| Radiometry | E_d | Downward irradiance [$\text{W m}^{-2} \text{nm}^{-1}$] |
| | E_u | Upward irradiance [$\text{W m}^{-2} \text{nm}^{-1}$] |
| | L_u | Upwelling radiance [$\text{W m}^{-2} \text{nm}^{-1} \text{sr}^{-1}$] |
| Data reduction | LN | Linear regression |
| | NL | Non-linear regression |
| Measurement depth | FST | Value at the beginning of each integration interval |
| | LST | Value at the end of each integration interval |
| | AvG | The averages of FST and LST values |
| | WGT | Value weighted based on the diffuse attenuation coefficient |

where n is the index of the radiometric profile in a pool of $N = 10$ independent ones that differ from each other for the random initialization of the deployment point of the virtual optical sensor at the surface.

Data regressions are performed in a layer determined by the depths -0.2 and -4 m. E_d , E_u and L_u data products are computed for a number of different settings, including: 1) deployment speeds of the optical system; 2) environmental conditions—*i.e.*, sky-radiance distribution as detailed Table 2, sea-surface statistics as detailed in Table 3, and marine water type as detailed in Table 5; 3) LN and NL regression methods; and 4) measurement depths as defined in Sec. 2.3.3. Specific analyses are presented to illustrate the independent effects of integration time (Sec. 3.2) and the additional influence of environmental perturbations (Sec. 3.3). A list of symbols for the identification of data products analyzed in this study is presented in Table 7.

3.2. The effects of integration time for a still sea and overcast illumination

A still sea and overcast illumination are considered in this section to exclude perturbations due to light focusing and the influence on the pressure gauge by surface waves. On this basis, Fig. 8 documents the data density in the water column (*i.e.*, the number of radiometric measurements per unit depth) when the optical system is deployed at $v_{\text{prf}} = 0.2 \text{ ms}^{-1}$. The inset of each panel shows the integration time as a function of depth [see also Table 6]. The Case-1, CDOM-dominated and NAP-dominated water cases are presented in the row panels from top to bottom, while results for E_d , E_u and L_u are from left to right. The sampling density varies from a maximum of about 40 m^{-1} for E_d close to the sea-surface in oligotrophic Case-1 waters, to a very few records per meter at -4 m depth for E_u and L_u in the CDOM-dominated case. Results document how the integration time increases with depth due to the lessening of the radiometric signal. A particular case is the E_d optical profile in Case-1 waters presented in Fig. 8(a), where the integration time remains constant because of the low attenuation coefficient. It is also noted that the integration time of E_u quickly settles to its maximum value for all the considered water types, as shown in Figs. 8(b), 8(e) and 8(h). This highlights the expected limitations in using the same radiometric thresholds to define the integration time for both E_d and E_u values, as specified in Table 6.

The percent differences affecting data products as determined through Eq. (15), are presented in Fig. 9. The first and the second column panels refer to E_{d0} and K_{E_d} , respectively. Equivalent statistical figures for E_u and L_u regression products are documented in the subsequent column pairs. The effects of integration time on the reduction of optical profiles for Case-1 and NAP-dominated waters show: 1) a low influence on E_d data products; and 2) larger percent biases for K_{E_u} and K_{L_u} than for E_{u0} and L_{u0} . Figs. 9(d) and 9(j) provide an example of how the effects of integration time on K_{E_u} increase with the deployment speed of the optical system. It is noted that the FST and the LST depth definitions lead to an overestimate and underestimate of K_{E_u} values, respectively, as a consequence of the long integration time illustrated in Fig. 8 for E_u data. A

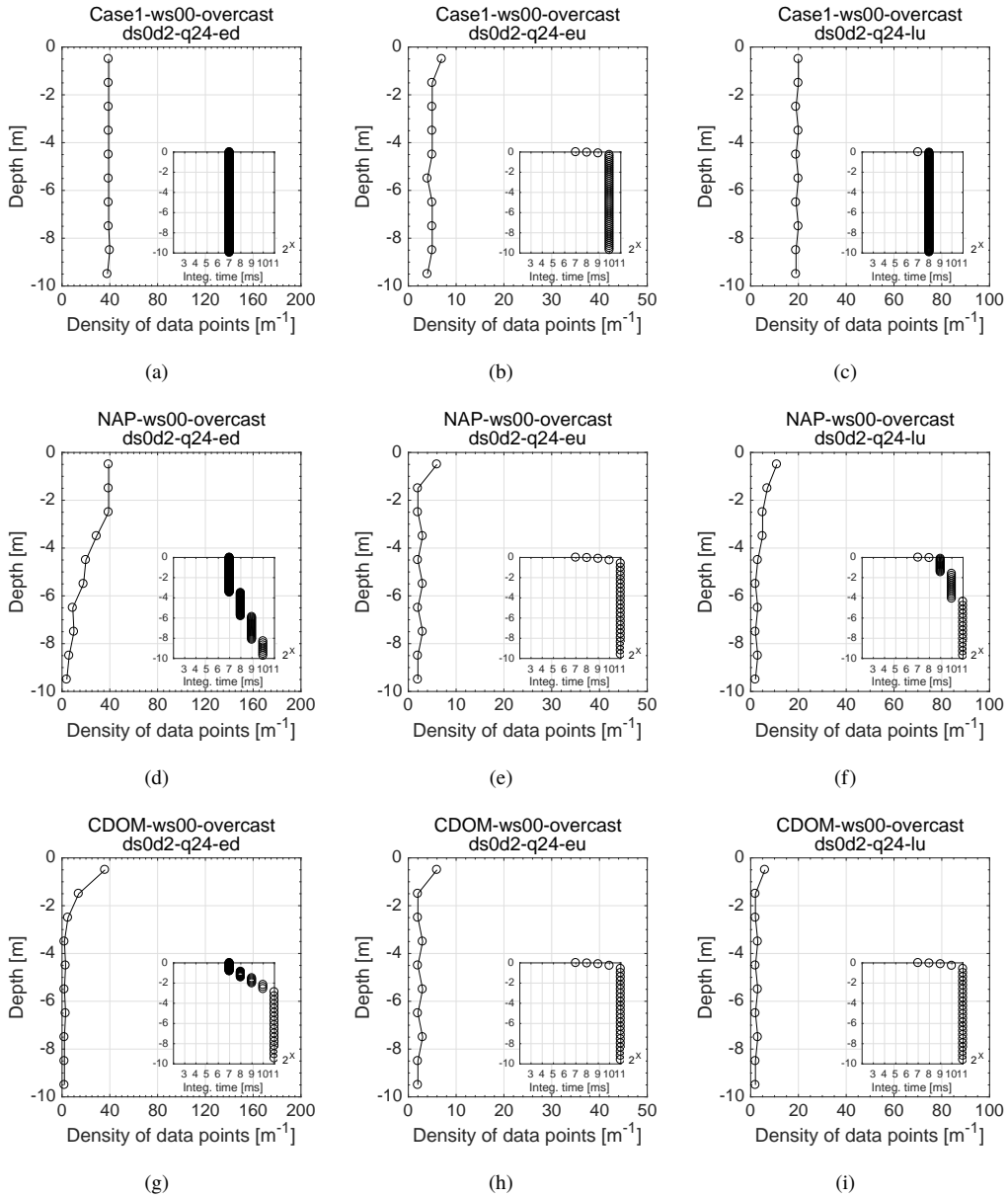


Fig. 8. Number of radiometric measurements per unit depth (*i.e.*, density of data) for overcast illumination and still sea surface. The deployment speed of the optical system is $v_{prf} = 0.2 \text{ ms}^{-1}$. The Case-1, CDOM-dominated and NAP-dominated water cases are ordered from top to bottom. Results for E_d , E_u and L_u are reported from the left to the right column panels. The integration time as a function of depth is displayed in each panel inset.

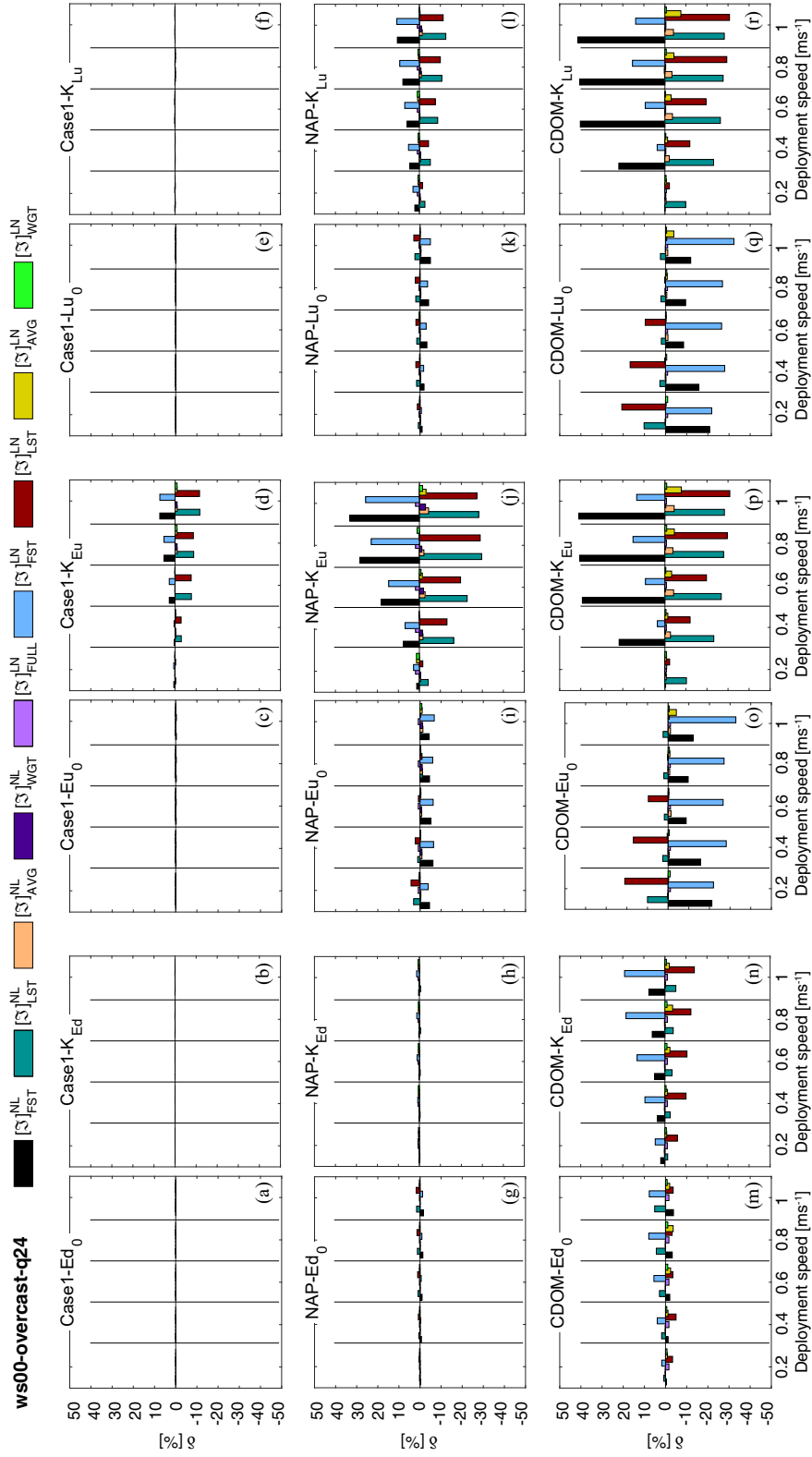


Fig. 9. Statistical figures from the comparison of regression products determined with Eq. (15) for a still sea and overcast sky.

similar tendency, but with smaller values, can be observed for K_{L_u} in Figs. 9(f) and 9(l). The effects of the integration time are slightly higher for NAP-dominated than for Case-1 waters. Figs. 9(i) and 9(k) indicate that the biases affecting E_{u0} and L_{u0} tend to be opposite to those affecting the attenuation coefficients (e.g., $[K_{L_u}]_{FST}^{NL} < 0$ corresponds to $[L_{u0}]_{FST}^{NL} > 0$).

Figures 9(m)–9(r) display an increase of the effects of the integration time for CDOM-dominated waters due to the high absorption coefficient [see Table 5]. The overall trends of the FST and LST depths to respectively overestimate and underestimate the diffuse attenuation coefficient are here confirmed, as well as the opposite sign of the offsets affecting the attenuation coefficients and subsurface radiometric values. Some heterogeneity clearly affects the tendencies of the offset values as a function of the deployment speed. It is then noted that the change of integration time with depth can itself be a perturbing component. This can be explained considering the separation of a generic pool of samples into disjoint sets. If all partitions have the same size, then the average of the mean values of individual subsets (group means) is equal to the mean value of the entire dataset (grand mean) [49]. In the case of subsets with different sizes, instead, the average of the group means can under- or over-estimate the dataset grand mean depending on how the subsets were constructed. A similar scenario can influence the reduction of optical profile data and slightly change the offsets with respect to the case of a constant integration time (details not presented).

3.3. The convoluted effects of integration time with environmental factors

A wavy sea surface ($v_{wnd} = 4 \text{ ms}^{-1}$) and clear sky ($\theta_{sun} = 30^\circ$) are now accounted for defining complementary conditions with respect to the still sea and overcast sky of the previous section. The aim is verifying how the effects of integration time on the reduction of optical profile data combine with environmental factors in a sampling scenario of practical interest for ocean color applications. As expected, the number of integrated radiometric values as a function of depth shown in Fig. 10 for clear sky conditions indicates an increase in data density due to the higher total irradiance with respect to the overcast case [see Fig. 8 and Table 2].

Following the same process applied for a steady sea surface and overcast sky, results obtained from simulated profiles for a wavy surface and clear sky are summarized in Fig. 11. Specifically, Fig. 11(a) indicates that the linear regression scheme produces $[E_{d0}]_{FULL}^{LN}$ values 10% lower than the reference ones $[E_{d0}]_{FULL}^{NL}$. This underestimate depends on the log-transformation of data affected by light focusing and defocusing effects as detailed in Section 2.3.4 and several published studies [14, 19, 23]. The manifold biases appearing in Fig. 11(b), instead, partially depend on the very low K_{E_d} values of the considered Case-1 water, which implies computing relative difference of quantities close to zero. This clearly confirms the difficulty to accurately determine the diffuse attenuation coefficient in oligotrophic waters with measurements performed in the subsurface layer. The example also shows that $[E_{d0}]_{DEF}^{LN} \sim [E_{d0}]_{FULL}^{NL}$, where the acronym DEF denotes any of the considered depths. As already observed for the overcast sky condition, the lower integration time in proximity of the sea surface has a larger influence on K_{E_d} than E_{d0} [see Table 8]. Figs. 11(c) and 11(e) document a negligible effect of the integration time on E_{u0} and L_{u0} . Instead Fig. 11(d) and partially Fig. 11(f) indicate that the FST and LST depth definitions induce a positive and a negative bias in both K_{E_u} and K_{L_u} values, respectively. The biases affecting the results for NAP-dominated waters presented in Figs. 11(g)–11(l), follow trends similar to those reported for Case-1 waters in Figs. 11(a)–11(f). The main difference is the lessening of the K_{E_d} biases—*cf.*, Fig. 11(b) and Fig. 11(h).

The CDOM-dominated case of Figs. 11(m)–11(r) attests the under- and the over-estimation of E_{d0} , E_{u0} and L_{u0} values when considering the FST and the LST measurement depths, respectively. It is also verified that this tendency mostly appears opposite to the bias reported for K_{E_d} , K_{E_u} and K_{L_u} , as observed for the overcast and still sea simulation case [see Fig. 9]. Namely, an underestimate of the subsurface value due to the FST depths corresponds to an overestimate of

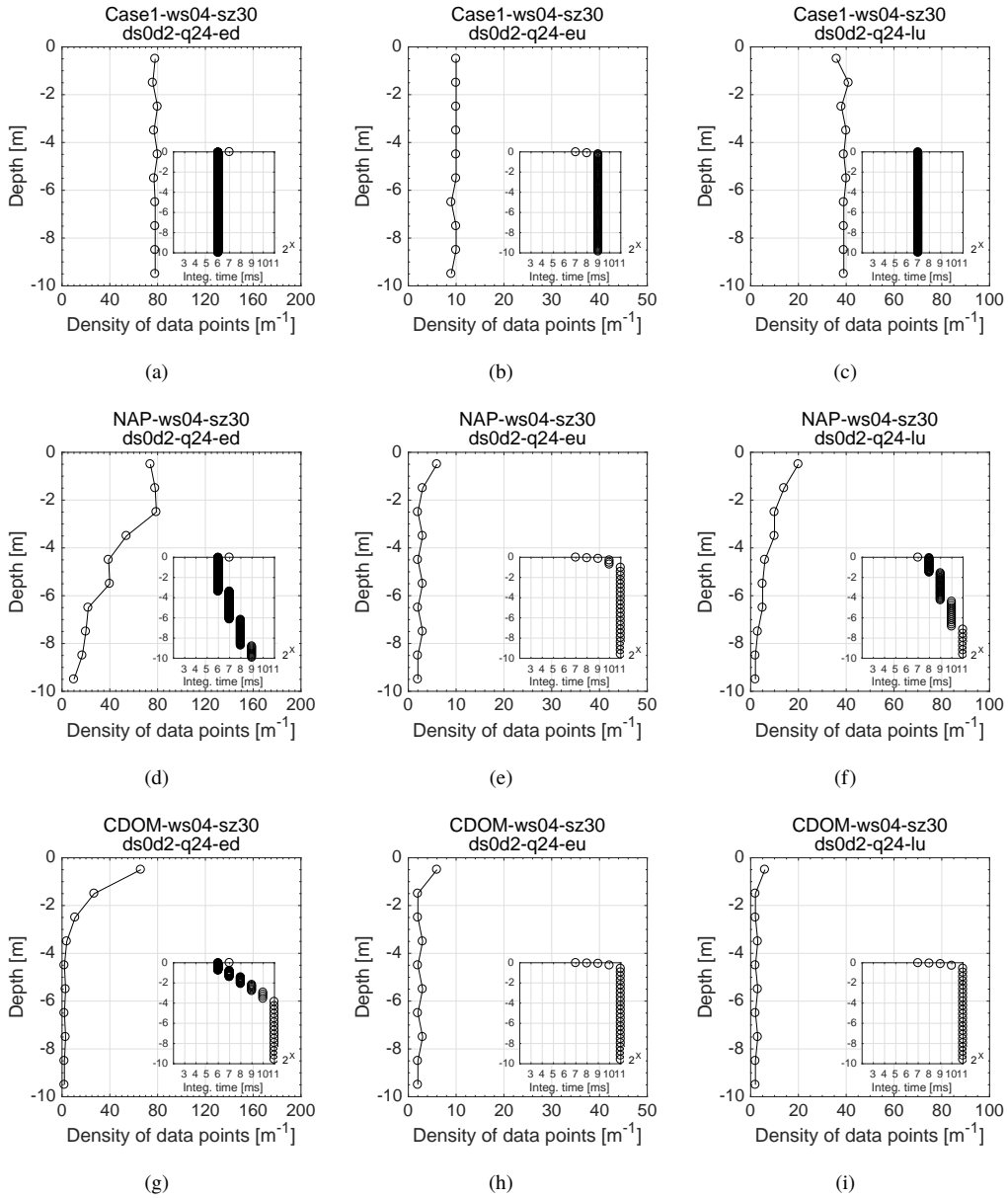


Fig. 10. As in Fig. 8, but considering a clear sky ($\theta_{\text{sun}} = 30^\circ$) and a wavy sea-surface ($v_{\text{wnd}} = 4 \text{ ms}^{-1}$).

Table 8. Values of Differences δ (Indicating both δ_{X_0} or δ_{K_X}) Determined with Eq.(15) and Values of the Related Standard Deviations σ (i.e., σ_X or σ_K), from Fig. 11 for the Avg and Wgr Depths. Values are Provided for the Different Water Types, Deployment Speeds and Regression Methods (i.e., NL and LN). The Number of Measurements per Unit Depth (i.e., Meas. Density) Refers to the Extrapolation Interval. The Cells in Shade of Gray Highlight Values Exceeding $\pm 1\%$.

| Water Type | Data Product | Depth Speed [ms ⁻¹] | Meas. Density [m ⁻¹] | δ_{X_0} | | | | | | δ_{K_X} | | | | | | | | | | | |
|------------|--------------|---------------------------------|----------------------------------|----------------|----------|--------------|-----------|----------|--------------|----------------|----------|--------------|-----------|----------|--------------|------|------|------|------|-----|-----|
| | | | | NL | | | LN | | | NL | | | LN | | | | | | | | |
| | | | | Avg μ | σ | Wgr σ | Avg μ | σ | Wgr σ | Avg μ | σ | Wgr σ | Avg μ | σ | Wgr σ | | | | | | |
| Case-1 | E_d | 0.2 | 74 | -0.1 | 0.1 | -0.1 | 0.1 | -0.6 | 0.2 | -0.6 | 0.2 | -3.2 | 4.4 | -3.2 | 4.4 | 22.8 | 5.3 | 22.8 | 5.3 | | |
| | | 0.6 | 25 | 0.0 | 0.2 | 0.0 | 0.2 | -0.2 | 0.3 | -0.2 | 0.3 | 1.2 | 8.8 | 1.2 | 8.8 | 39.3 | 15.0 | 39.3 | 15.0 | | |
| | | 1.0 | 15 | 0.0 | 0.2 | 0.0 | 0.2 | -0.4 | 0.4 | -0.4 | 0.4 | -3.9 | 11.6 | -3.9 | 11.6 | 29.6 | 17.5 | 29.6 | 17.5 | | |
| | E_u | 0.2 | 9 | 0.0 | 0.0 | 0.0 | 0.0 | 0.0 | 0.0 | 0.0 | 0.0 | 0.0 | 0.1 | 0.4 | 0.1 | 0.4 | 0.1 | 0.4 | 0.1 | 0.4 | |
| | | 0.6 | 3 | 0.0 | 0.0 | 0.0 | 0.0 | 0.0 | 0.0 | 0.0 | 0.0 | 0.0 | -0.1 | 0.7 | -0.1 | 0.7 | 0.0 | 0.7 | 0.0 | 0.7 | |
| | | 1.0 | 2 | 0.0 | 0.0 | 0.0 | 0.0 | 0.0 | 0.0 | 0.0 | 0.0 | 0.0 | -1.2 | 0.5 | -1.2 | 0.5 | -1.2 | 0.5 | -1.2 | 0.5 | |
| NAP | L_u | 0.2 | 37 | 0.0 | 0.0 | 0.0 | 0.0 | 0.0 | 0.0 | 0.0 | 0.0 | 0.0 | 0.2 | 0.0 | 0.0 | 0.2 | 0.0 | 0.2 | 0.0 | 0.2 | |
| | | 0.6 | 12 | 0.0 | 0.0 | 0.0 | 0.0 | 0.0 | 0.0 | 0.0 | 0.0 | 0.0 | 0.1 | 0.3 | 0.1 | 0.3 | 0.1 | 0.3 | 0.1 | 0.3 | |
| | | 1.0 | 7 | 0.0 | 0.0 | 0.0 | 0.0 | 0.0 | 0.0 | 0.0 | 0.0 | 0.0 | 0.1 | 0.9 | 0.1 | 0.9 | 0.1 | 0.9 | 0.1 | 0.9 | |
| | E_d | 0.2 | 67 | -0.2 | 0.3 | -0.2 | 0.3 | -0.4 | 0.3 | -0.4 | 0.3 | -0.4 | 0.6 | -0.4 | 0.6 | -0.4 | 0.6 | 0.2 | 0.5 | 0.2 | 0.5 |
| | | 0.6 | 22 | -0.1 | 0.2 | -0.1 | 0.2 | -0.1 | 0.3 | -0.1 | 0.3 | -0.2 | 0.4 | -0.2 | 0.4 | -0.2 | 0.4 | 0.8 | 0.6 | 0.8 | 0.6 |
| | | 1.0 | 14 | 0.2 | 0.3 | 0.2 | 0.3 | -0.1 | 0.4 | -0.1 | 0.4 | 0.3 | 0.5 | 0.3 | 0.5 | 1.0 | 0.7 | 1.0 | 0.7 | | |
| CDOM | E_u | 0.2 | 3 | -0.4 | 0.4 | -0.4 | 0.4 | 0.2 | 0.4 | 0.2 | 0.4 | -0.8 | 0.5 | -0.7 | 0.5 | 1.0 | 0.5 | 1.0 | 0.5 | | |
| | | 0.6 | 1 | -1.0 | 0.3 | -0.9 | 0.3 | -0.6 | 0.3 | -0.6 | 0.3 | -3.2 | 0.8 | -2.6 | 0.8 | -1.9 | 0.7 | -1.4 | 0.7 | | |
| | | 1.0 | 1 | -1.4 | 0.3 | -1.3 | 0.3 | -1.1 | 0.2 | -1.0 | 0.3 | -4.7 | 0.8 | -3.5 | 0.8 | -3.5 | 0.6 | -2.2 | 0.6 | | |
| L_u | 0.2 | 13 | -0.1 | 0.1 | -0.1 | 0.1 | 0.3 | 0.1 | 0.3 | 0.1 | 0.3 | -0.4 | 0.3 | -0.4 | 0.3 | 0.7 | 0.2 | 0.7 | 0.2 | | |
| | 0.6 | 4 | -0.2 | 0.2 | -0.2 | 0.2 | 0.3 | 0.2 | 0.3 | 0.2 | -0.4 | 0.3 | -0.4 | 0.3 | 0.7 | 0.4 | 0.7 | 0.4 | | | |
| | 1.0 | 3 | -0.3 | 0.3 | -0.3 | 0.3 | 0.2 | 0.2 | 0.1 | 0.2 | -0.7 | 0.6 | -0.6 | 0.6 | 0.5 | 0.4 | 0.5 | 0.4 | | | |
| CDOM | E_d | 0.2 | 25 | -0.3 | 0.8 | -0.3 | 0.8 | -0.8 | 1.0 | -0.7 | 1.0 | -0.3 | 1.2 | -0.3 | 1.2 | -0.3 | 1.1 | -0.2 | 1.1 | | |
| | | 0.6 | 9 | -0.2 | 0.9 | -0.2 | 0.9 | -0.9 | 0.7 | -0.6 | 0.7 | -0.1 | 1.1 | 0.0 | 1.1 | -0.5 | 0.7 | -0.2 | 0.7 | | |
| | | 1.0 | 5 | 0.8 | 1.1 | 0.8 | 1.1 | -1.4 | 1.2 | -0.7 | 1.2 | 1.0 | 1.3 | 1.1 | 1.3 | -1.2 | 1.0 | -0.4 | 1.0 | | |
| | E_u | 0.2 | 3 | 0.1 | 3.1 | -0.1 | 3.1 | 0.7 | 2.0 | 0.2 | 2.0 | -0.6 | 2.1 | -0.2 | 2.1 | 0.3 | 0.7 | 0.3 | 0.7 | | |
| | | 0.6 | 1 | -1.6 | 1.9 | -0.5 | 1.9 | 0.2 | 1.8 | 0.2 | 1.8 | -4.3 | 2.2 | -0.8 | 2.3 | -2.5 | 0.9 | 0.1 | 0.9 | | |
| | | 1.0 | 1 | -1.8 | 1.5 | -1.0 | 1.7 | -3.3 | 1.6 | -0.3 | 1.6 | -5.1 | 1.9 | -1.6 | 2.0 | -6.9 | 1.1 | -0.4 | 1.2 | | |
| L_u | 0.2 | 3 | 0.8 | 3.2 | 0.4 | 3.2 | 1.2 | 1.9 | 0.6 | 1.9 | -0.2 | 2.2 | 0.0 | 2.2 | 0.4 | 0.6 | 0.5 | 0.6 | | | |
| | 0.6 | 1 | -1.8 | 1.2 | -0.8 | 1.2 | -0.7 | 2.7 | -0.8 | 2.7 | -4.1 | 1.9 | -0.5 | 1.8 | -3.0 | 1.3 | -0.5 | 1.4 | | | |
| | 1.0 | 1 | -1.9 | 1.6 | -0.9 | 1.8 | -3.6 | 1.9 | -0.6 | 1.8 | -4.9 | 1.9 | -1.1 | 2.2 | -6.8 | 1.4 | -0.4 | 1.5 | | | |

the diffuse attenuation coefficient. Opposite results can be observed with the LST depths. It is finally noted that $[\delta_{\mathfrak{J}}]_{\text{WGT}}^{\text{NL}}$ as well as $[\delta_{\mathfrak{J}}]_{\text{AVG}}^{\text{NL}}$ show the best data reduction performances among the various depth definitions. This highlights the importance to adopt a proper determination of measurement depth to limit the impact of perturbations due to integration time.

In view of supporting a more comprehensive analysis of results, the mean values (generically indicated as δ) of computed $\delta_{\mathfrak{X}_0}$ and $\delta_{K_{\mathfrak{R}}}$ values displayed in Fig. 11, are also summarized in Table 8 together with their standard deviations σ for the AVG and WGT depths exhibiting best regression performances. Values of δ or σ outside the ideal target interval of $\pm 1\%$ are highlighted in shade of gray. By remarking that these results refer to simulated measurements from 24-bit radiometers, values of δ or σ outside the selected interval are observed for both NL and LN regression products and in particular: 1) for E_d , E_u and L_u in CDOM-dominated waters for most of the deployment speeds; and 2) for E_u in NAP-dominated waters with deployment speed of 1 ms^{-1} . It is also observed that δ and σ tend to be more pronounced with a decrease of the density of simulated measurements in the regression layer, which is naturally associated to an increase of the deployment speed. When specifically looking at results for $K_{\mathfrak{R}}$, in addition to the cases already identified for E_d , E_u and L_u affected by a relatively low density of simulated measurements, both δ and σ determined for K_{E_d} largely exceed the $\pm 1\%$ limit in clear waters as a result of wave perturbations.

4. Discussion

Building on previous analyses, this section progresses the discussion towards elements of practical relevance for actual field measurements. In particular, it addresses: 1) the impact of the spectral dependence of radiometric quantities on regression products; 2) the performance of hyperspectral radiometers commonly used in the field; and finally 3) the application of the multicasting technique to enhance precision of regression products.

4.1. Spectral dynamics and integration time

Radiance and irradiance from natural waters vary spectrally. An ideal measurement solution would require that the integration time is optimized for each wavelength, but technological constraints impose limitations. The integration time is generally determined using the maximum radiometric value across the measured spectrum in agreement with the scheme detailed in Fig. 6. Nevertheless, the sensor spectral response is low in the blue and high in the red, as well as the spectral distribution of light from natural waters is low in the red and highly variable in the blue. Because of this, the portions of measured spectrum away from the wavelength at which the integration time is determined, are characterized by a signal-to-noise ratio (SNR) decreasing with the signal amplitude and consequently may exhibit increasing uncertainties.

A case study equivalent to that considered in Fig. 11 has then been performed for a signal 10 times lower than that previously applied. These additional results are presented in Fig. 12.

In other words, in view of investigating the impact of signal dynamics, the two analyses of Fig. 11 and Fig. 12 refer to the same integration times, but the latter is based on a lower signal. Results, which do not exhibit major differences with respect to the ideal case presented in Fig. 11, indicate that even a non favorable integration time, such as that applied to data away from maxima, does not appreciably affect the radiometric products when measurements benefit of a high SNR. It is in fact recalled that both analyses rely on the assumption of a 24-bit digitization.

4.2. Performance of commonly used in-water hyperspectral field radiometers

So far this study has neglected the latency time, which implies the assumption of a null delay between the end of a measurement and the start of the successive one. This delay is due to a number of actions comprising the transfer of the charge accumulated in the elements of the photo-detector array, its conversion to a digital value and the handling of this latter. The overall

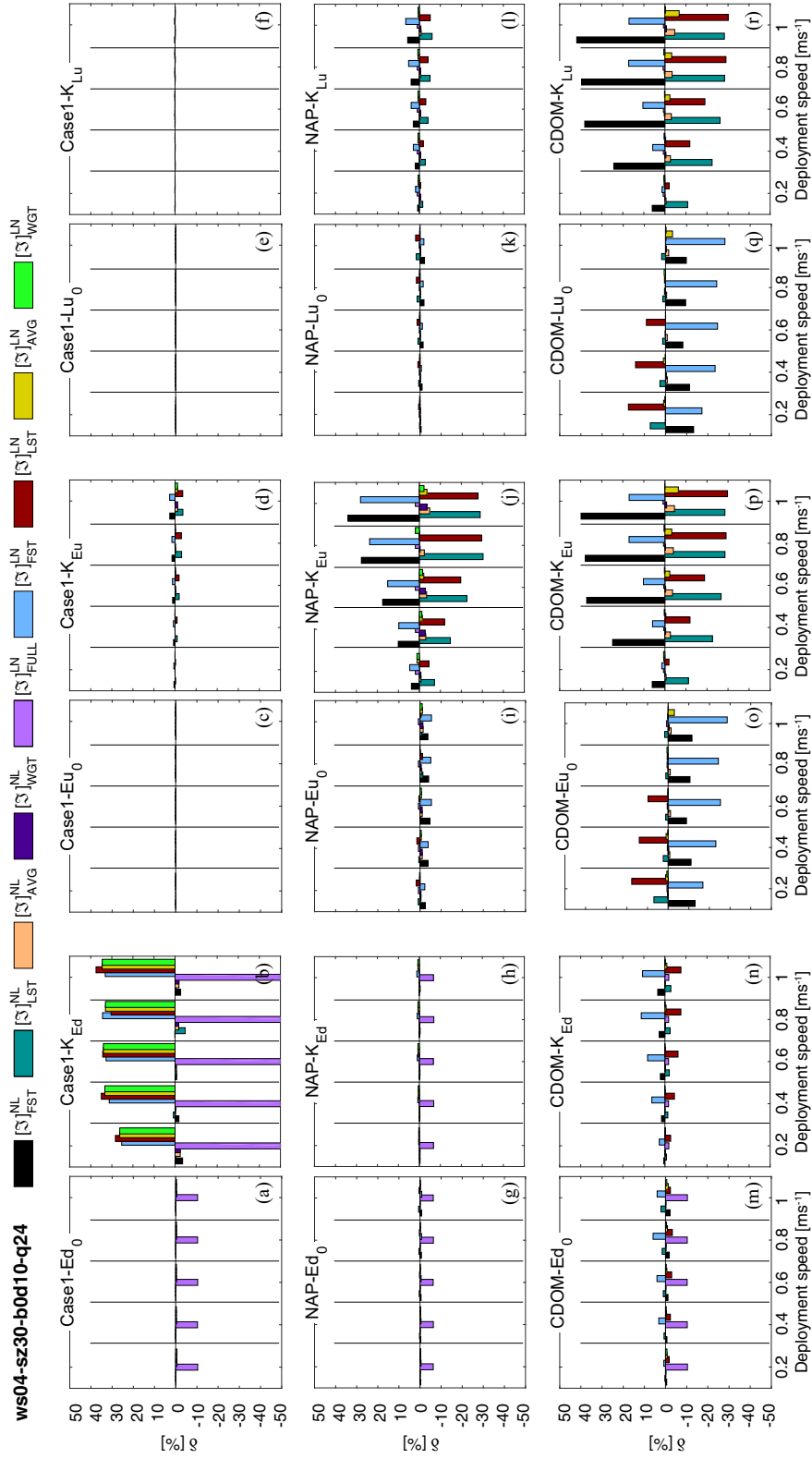


Fig. 12. As in Fig. 11, but for a signal 10 times lower than that applied for the determination of the integration time.

delay is not related to the collection of photons and can be significant in current field radiometers when compared to the integration time. Latency times of 200–300ms, varying from unit to unit, were observed for HyperOCRs. These latency times are responsible for a reduction of data points in radiometric profiles that may lower the accuracy of regression results. The number of data in the radiometric profiles can further decrease due to the use of an internal shutter to determine the dark-signal. In particular, HyperOCRs are often programmed to collect 1 dark-signal after 5 sequential radiometric measurements.

An additional source of uncertainty is a SNR lower than that insofar considered in this study. Specifically, HyperOCRs digitize the radiometric signal with a 16-bit ADC. With this respect, Table 9 summarizes the SNR applied for sub-surface data simulated as a function of water type for the 16- and 24-bits systems. Excluding any source of uncertainty other than the digitization one, a specific analysis is presented to document the ability to actually mimic HyperOCRs profile data considering 16-bit ADC and fully accounting for both a latency time of 250 ms and the capability of regularly measuring the dark-signal with the internal shutter. Equivalent to the 24-bit analysis presented in Sec. 4.1, a noise sampled from a normal distribution with standard deviation of 10 digital counts has been added to the digitized radiometric values. This standard deviation was actually determined from measurements of the dark signal performed with HyperOCR radiometers operated in thermally stable conditions.

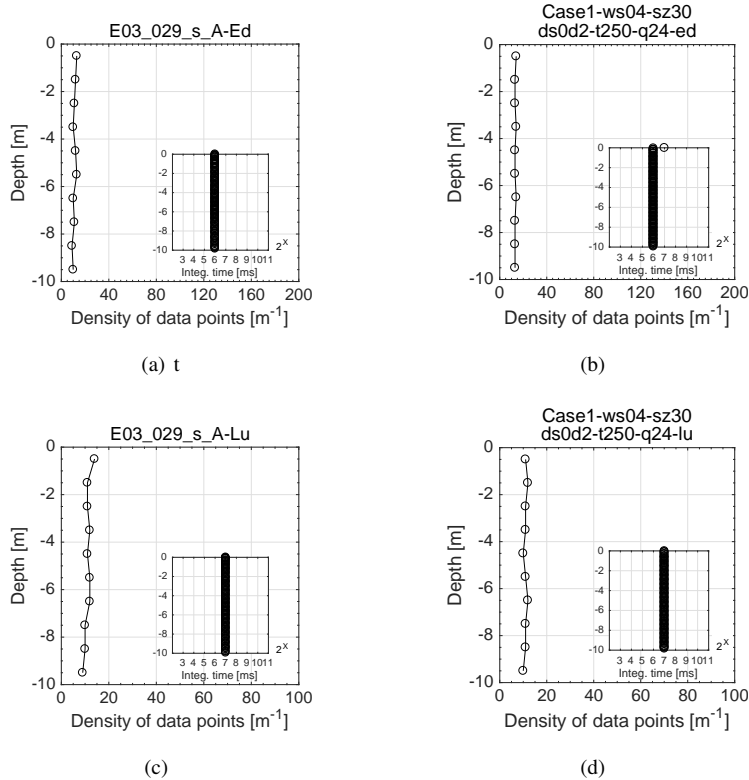


Fig. 13. Number of simulated data per unit depth obtained during clear sky with latency time of 250ms and 1 dark-signal recording after every 5 successive measurements. E_d and L_u results are presented in the top and bottom row panels, respectively. Experimental and simulated values (referring to $v_{prf} = 0.2 \text{ ms}^{-1}$, $v_{wnd} = 4 \text{ ms}^{-1}$, $\theta_{sun} = 30^\circ$, $a = 0.01 \text{ m}^{-1}$ and $b = 0.09 \text{ m}^{-1}$) are displayed in the left and right column, respectively.

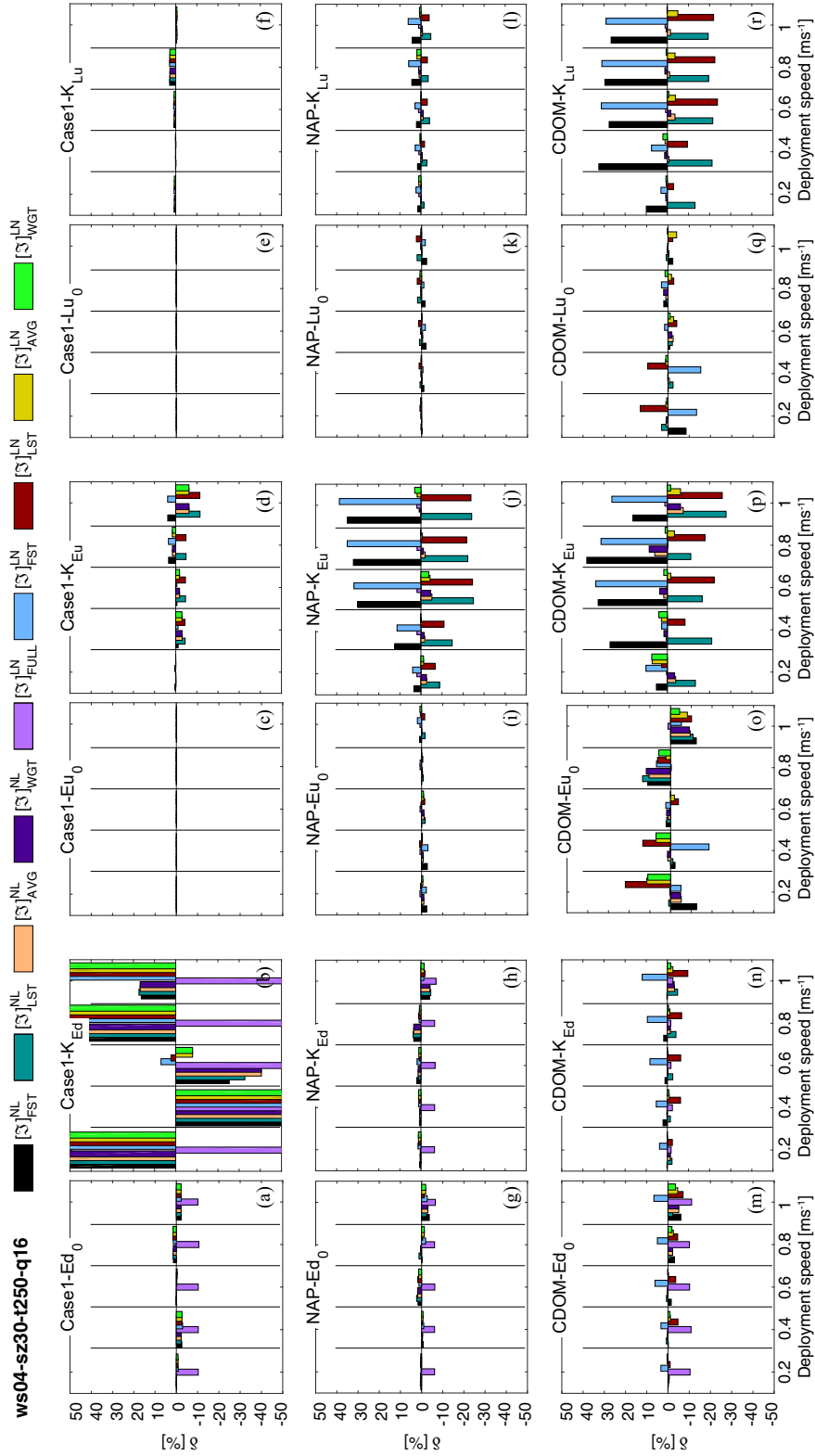


Fig. 14. As in Fig. 11, but considering 16-bit ADC and accounting for both the latency time of 250ms and dark-signal recording.

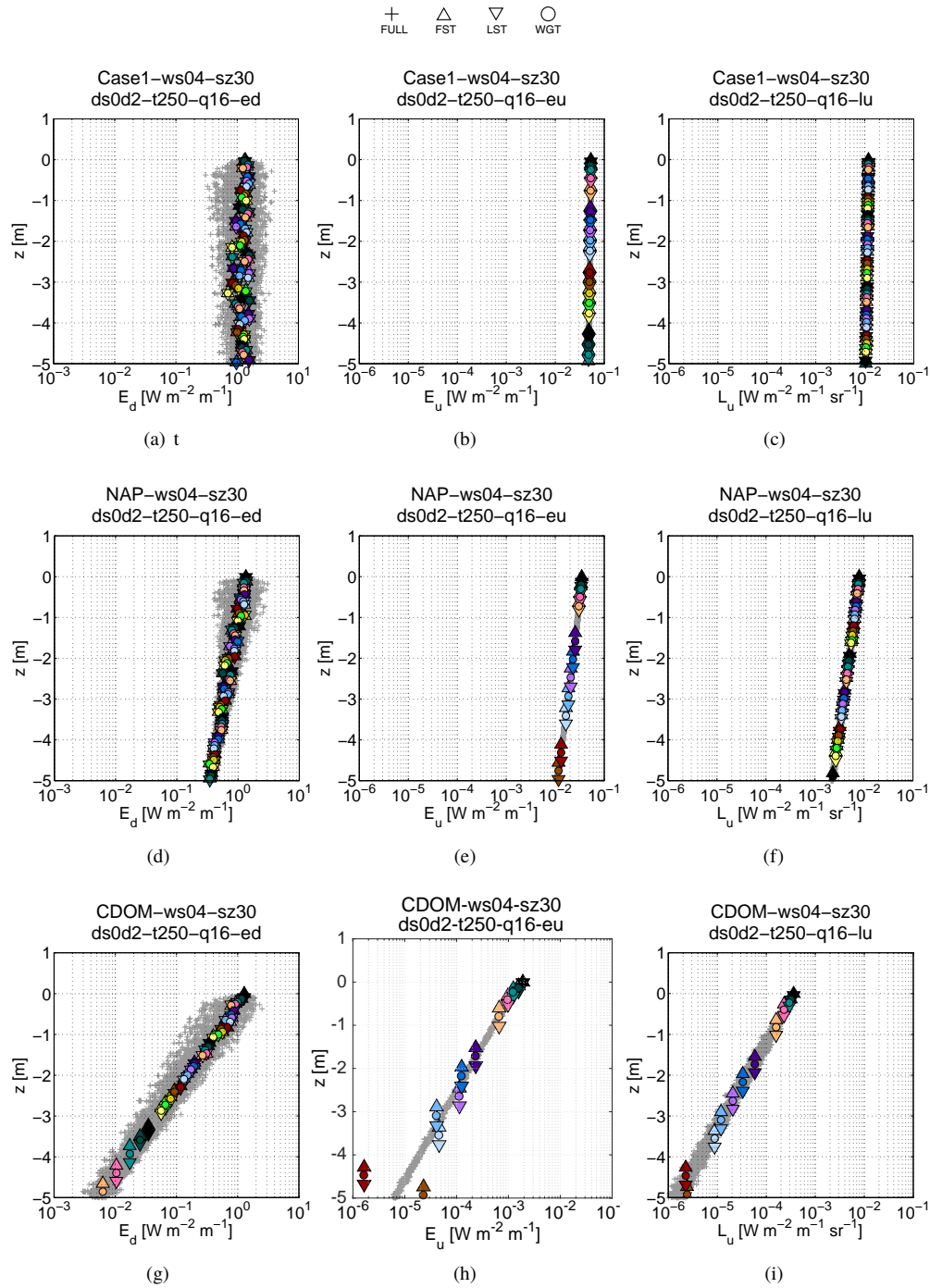


Fig. 15. Virtual optical profiles for Case-1, NAP and CDOM-dominated waters, considering 16-bit ADC, latency time of 250ms and dark-signal recording, and assuming a clear sky and a wind-driven sea surface. The deployment speed is $v_{prf} = 0.2 \text{ ms}^{-1}$. E_d , E_u and L_u are in the row panels from top to bottom. FULL resolution points are denoted by the + symbol in shade of gray. The integrated values are labeled as Δ , ∇ and \circ for the FST, LST, and WGT depths, respectively.

Table 9. Values of the Signal-to-noise-ratio (SNR) Characterizing the Sub-surface Radiometric Quantities Simulated for Different Water Types and for 16- and 24-bit Systems.

| | 16 Bits | | | 24 Bits | | |
|-------|----------|----------|----------|----------|----------|----------|
| | E_d | E_u | L_u | E_d | E_u | L_u |
| Case1 | 2.60E+03 | 1.20E+03 | 1.70E+03 | 6.60E+05 | 3.20E+05 | 4.30E+05 |
| NAP | 2.60E+03 | 1.10E+03 | 1.40E+03 | 6.40E+05 | 2.80E+05 | 3.50E+05 |
| CDOM | 2.60E+03 | 9.60E+01 | 5.00E+02 | 6.50E+05 | 2.50E+04 | 1.30E+05 |

Figure 13 displays the density of L_u and E_d radiometric data obtained from actual HyperOCR radiometers and the corresponding simulated values. Notably, experimental and simulated results exhibit very close densities of about 10 measurements per meter.

Figure 14 shows the equivalent analyses presented in Fig. 11. Results indicate the impact of an expected lowering in performance of radiometric measurements due to a decrease of the SNR implicit of the use of a 16-bit digitization alternative to the 24-bit one. The decreased measurement quality is more evident across the various depth definitions for E_u and L_u in CDOM-dominated waters in agreement with the lower SNR values shown in Table 9. In particular, the quality of the data indicates the difficulty to determine radiometric products for E_u in highly absorbing waters as a result of the assumption of equal sensitivity for both E_d and E_u . This is clearly illustrated by the sample virtual profiles displayed in Fig. 15. A higher sensitivity would definitively increase the measurement accuracy of both L_u and E_u beyond that documented in Fig. 14.

4.3. Multicast profiles

Enhancing the density of optical profile data improves the precision of regression results in the presence of perturbations that do not induce a systematic under or overestimation. An example is the use of the multicasting scheme that combines multiple casts into a single profile. This was shown to lessen the sea-surface focusing and defocusing effects in regression products from measurements performed at fixed acquisition rate [11, 19]. Here, by considering profiles performed at variable acquisition rate implicit of the application of a variable integration time, a new analysis is presented for 16-bit systems to illustrate the impact of data density on regression products.

Examples of single-cast and multicast profiles are displayed in Fig. 15 and Fig. 16, respectively. In both cases, notable is the impact of integration time: integrated values exhibit a lower dependence to wave perturbations with respect to full resolution data of Fig. 15(a) and Fig. 16(a). While statistical regression results for the single-cast case have been already presented in Fig. 14, those related to the multicast case are summarized in Fig. 17. The comparison between the two analyses confirms that increasing the number of data records per unit depth through the multicasting scheme, improves the precision of regression products by minimizing the effects of environmental perturbations.

In view of providing guidelines for profiling with hyperspectral systems, Tables 10, 11 and 12 summarize statistical analysis for E_d , E_u and L_u regression products, respectively, for the single-cast and multicasting schemes, as well as for different water types and various deployment speeds. This analysis is restricted to WGT depths and to the realistic case featuring a 16-bit ADC, latency time of 250 ms and dark-signal recording. It is specified that: 1) results are always obtained from a pool of 10 independent samples; and 2) each sample of the pool is an individual cast in the single-cast scheme, while alternatively it refers to the combination of 5 or 10 casts in the multicasting one.

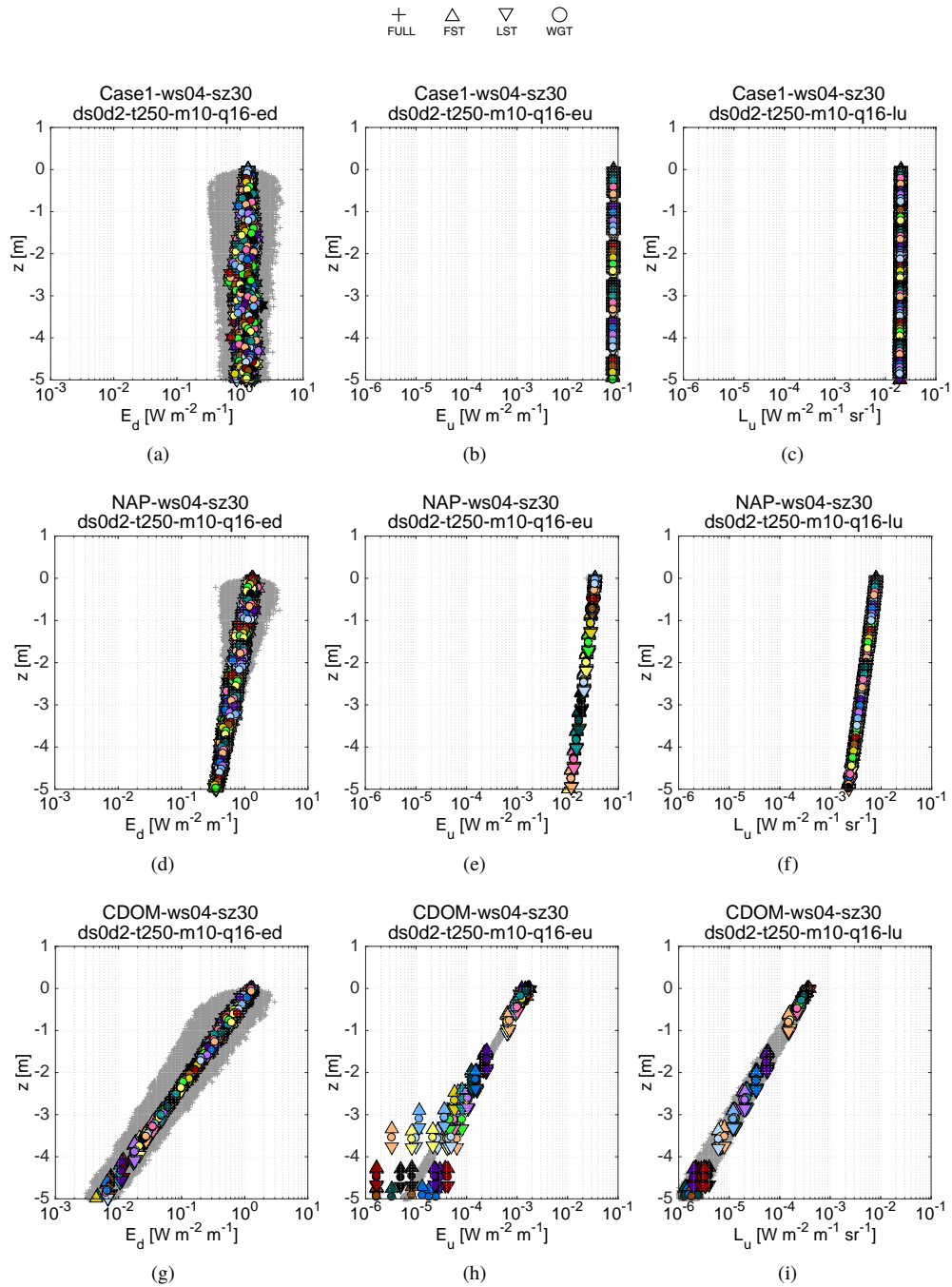


Fig. 16. As in Fig. 15, but adopting the multicasting scheme with 10 independent casts combined into a single profile.

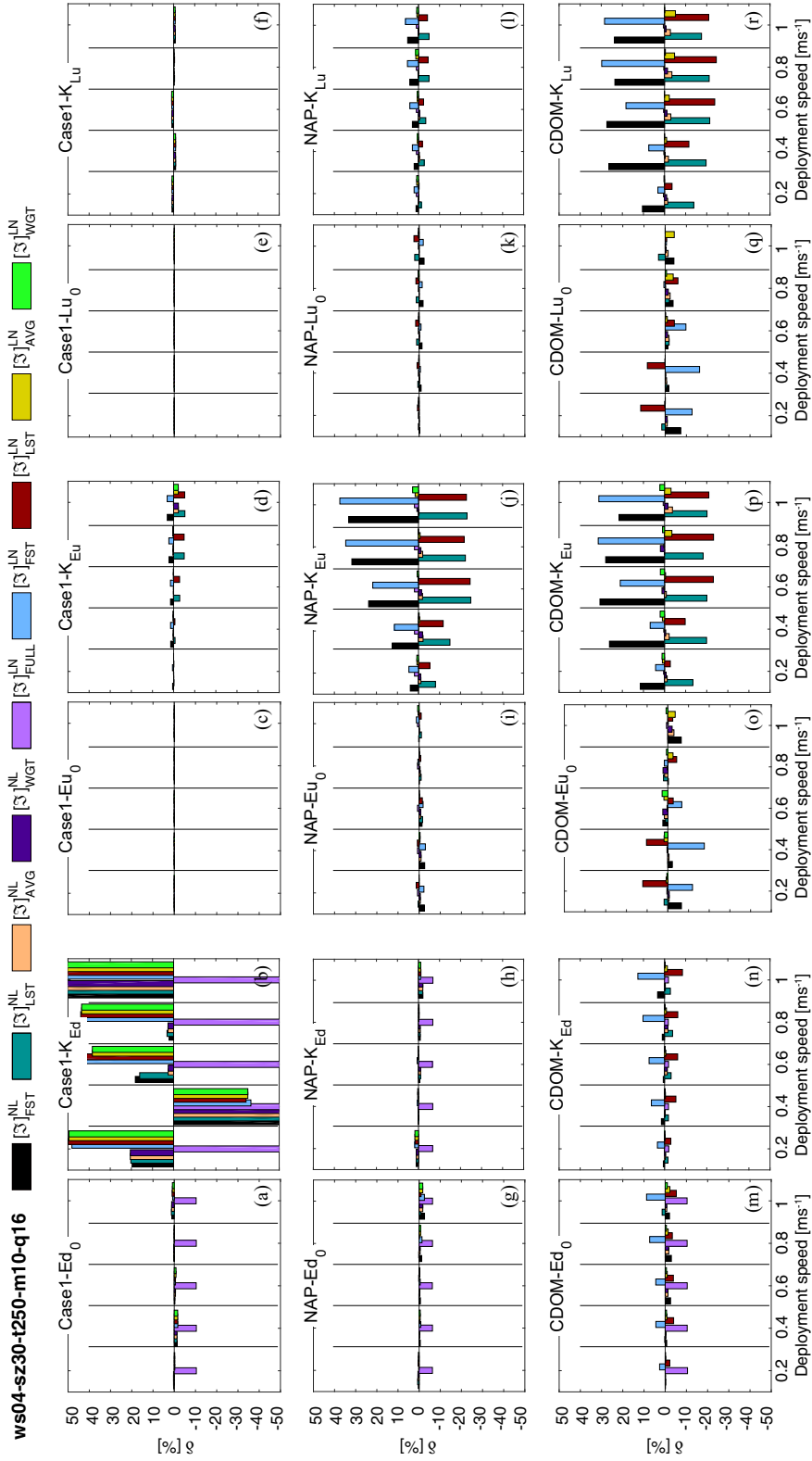


Fig. 17. As in Fig. 14, but adopting the multicasting scheme with 10 optical profiles.

Table 10. E_d Regression Products Determined Accounting for 16-bit ADC, Latency Time of 250ms and Dark-signal Recording. Both the Single-cast and the Multicast Profiles (the Latter Built with 5 or alternatively 10 Casts) are Considered. Statistical Figures are Provided for the Sole Wgr Depths, both the NL and the LN Regression Methods, the Various Water Types and Deployment Speeds of 0.2, 0.6 and 1.0 ms^{-1} . Symbols μ , CV, δ and σ Refer to the Mean of Regression Products, their Coefficient of Variation, the Percent Differences with Respect to Reference Values Determined with Eq.15 and the Related Standard Deviations, respectively. It is further Mentioned that Results Refer to a Pool of 10 Samples for each Case. The Mean Density of Measurements is also Reported to Identify cases Leading to a Better Determination of Regression Products. The Cells in Shade of Gray Highlight Values Exceeding $\pm 2\%$.

| Water Type | Depl. Speed [ms^{-1}] | Meas. Density [m^{-1}] | E_{d0} | | | LN | | | K_{E_d} | | | LN | | | | | | |
|------------|----------------------------------|-----------------------------------|----------|------|----------|----------|----------|----------|-----------|----------|----------|-------|-------|----------|----------|-------|--------|-------|
| | | | μ | CV | δ | μ | CV | δ | μ | CV | δ | μ | CV | δ | σ | | | |
| Case-1 | 0.2 | 1 | 1.39E+00 | 6.1 | -2.1 | 6.1 | 1.39E+00 | 6.6 | -1.6 | 6.5 | 2.64E-02 | 129.3 | -76.6 | 227.5 | 3.06E-02 | 116.1 | -105.1 | 236.1 |
| | | 5 | 1.36E+00 | 1.6 | -0.1 | 1.4 | 1.38E+00 | 1.6 | 0.6 | 1.5 | 1.59E-02 | 57.8 | -15.4 | 66.4 | 1.92E-02 | 52.0 | -39.5 | 70.9 |
| | | 10 | 1.37E+00 | 1.4 | -0.8 | 1.3 | 1.36E+00 | 1.3 | -0.2 | 1.3 | 2.01E-02 | 56.8 | -43.8 | 81.4 | 2.39E-02 | 46.1 | -72.2 | 77.2 |
| | 0.6 | 1 | 1.36E+00 | 6.3 | -0.3 | 5.9 | 1.36E+00 | 6.1 | 0.1 | 5.6 | 5.70E-03 | 527.9 | 89.6 | 301.6 | 8.10E-03 | 359.5 | 64.6 | 286.9 |
| | | 5 | 1.37E+00 | 2.5 | -0.9 | 2.5 | 1.37E+00 | 2.8 | -0.5 | 2.7 | 1.81E-02 | 61.3 | -33.8 | 80.1 | 2.18E-02 | 55.0 | -61.4 | 86.5 |
| | | 10 | 1.35E+00 | 1.1 | 0.8 | 1.2 | 1.35E+00 | 1.1 | 1.2 | 1.1 | 1.01E-02 | 58.2 | 26.7 | 45.1 | 1.41E-02 | 42.0 | -1.6 | 45.8 |
| 1.0 | 1 | 1.33E+00 | 10.6 | 2.1 | 10.2 | 1.33E+00 | 10.1 | 2.0 | 9.7 | 6.00E-04 | 8238.9 | 162.0 | 487.8 | 7.30E-03 | 647.5 | 83.0 | 450.9 | |
| | 5 | 1.39E+00 | 2.6 | -1.8 | 2.7 | 1.38E+00 | 2.8 | -1.3 | 2.9 | 2.22E-02 | 80.6 | -47.6 | 116.7 | 2.61E-02 | 73.4 | -73.6 | 124.8 | |
| | 10 | 1.37E+00 | 3.5 | -0.7 | 3.3 | 1.37E+00 | 3.5 | -0.5 | 3.4 | 1.87E-02 | 95.9 | -26.9 | 132.3 | 2.40E-02 | 73.6 | -66.5 | 128.5 | |
| NAP | 0.2 | 1 | 1.33E+00 | 4.3 | -0.6 | 4.2 | 1.31E+00 | 2.2 | 0.8 | 2.4 | 1.11E+00 | 4.2 | -0.9 | 4.7 | 1.10E+00 | 0.5 | 0.1 | 1.4 |
| | | 5 | 1.31E+00 | 1.9 | 1.2 | 2.1 | 1.32E+00 | 1.3 | 0.3 | 1.7 | 1.08E+00 | 1.9 | 1.6 | 1.9 | 1.10E+00 | 0.4 | 0.1 | 0.9 |
| | | 10 | 1.32E+00 | 1.4 | 0.3 | 1.0 | 1.32E+00 | 0.6 | -0.2 | 1.2 | 1.09E+00 | 1.7 | 0.7 | 1.2 | 1.10E+00 | 0.1 | -0.2 | 0.7 |
| | 0.6 | 1 | 1.32E+00 | 4.5 | 0.2 | 4.5 | 1.32E+00 | 4.1 | 0.6 | 4.3 | 1.10E+00 | 4.9 | 0.1 | 4.8 | 1.10E+00 | 1.4 | 0.2 | 1.6 |
| | | 5 | 1.31E+00 | 1.6 | 0.6 | 1.5 | 1.31E+00 | 1.9 | 0.9 | 1.9 | 1.10E+00 | 1.5 | 0.2 | 1.4 | 1.10E+00 | 0.6 | 0.3 | 0.6 |
| | | 10 | 1.32E+00 | 1.4 | 0.1 | 1.4 | 1.30E+00 | 1.5 | 1.3 | 1.5 | 1.11E+00 | 1.8 | -0.5 | 1.8 | 1.10E+00 | 0.5 | 0.3 | 0.5 |
| 1.0 | 1 | 1.37E+00 | 10.9 | -4.3 | 12.2 | 1.32E+00 | 5.4 | 0.2 | 6.3 | 1.14E+00 | 7.6 | -3.7 | 8.6 | 1.10E+00 | 2.3 | -0.2 | 3.2 | |
| | 5 | 1.31E+00 | 3.3 | 1.3 | 3.1 | 1.30E+00 | 2.9 | 1.5 | 3.3 | 1.10E+00 | 3.4 | 0.5 | 3.1 | 1.10E+00 | 0.8 | 0.6 | 1.2 | |
| | 10 | 1.33E+00 | 3.9 | -0.9 | 4.1 | 1.33E+00 | 0.9 | -0.6 | 0.9 | 1.10E+00 | 3.6 | -0.2 | 3.8 | 1.10E+00 | 0.3 | -0.3 | 0.6 | |
| CDOM | 0.2 | 1 | 1.37E+00 | 2.8 | -1.8 | 3.0 | 1.37E+00 | 2.3 | -1.8 | 2.5 | 2.66E-01 | 5.3 | -1.8 | 5.5 | 2.68E-01 | 4.1 | -2.8 | 4.4 |
| | | 5 | 1.35E+00 | 1.5 | 0.2 | 1.4 | 1.35E+00 | 1.0 | -0.1 | 0.9 | 2.61E-01 | 3.4 | 0.3 | 3.2 | 2.66E-01 | 2.5 | -1.3 | 2.4 |
| | | 10 | 1.36E+00 | 1.2 | -0.9 | 1.2 | 1.36E+00 | 1.2 | -0.8 | 1.2 | 2.66E-01 | 2.0 | -1.9 | 1.9 | 2.69E-01 | 1.7 | -2.8 | 1.7 |
| | 0.6 | 1 | 1.33E+00 | 4.0 | 1.0 | 4.1 | 1.34E+00 | 3.4 | 0.8 | 3.5 | 2.57E-01 | 5.8 | 1.1 | 6.0 | 2.61E-01 | 4.4 | -0.3 | 4.6 |
| | | 5 | 1.34E+00 | 1.2 | 0.7 | 1.1 | 1.35E+00 | 1.5 | 0.4 | 1.4 | 2.58E-01 | 2.0 | 1.2 | 2.0 | 2.62E-01 | 1.6 | -0.4 | 1.4 |
| | | 10 | 1.35E+00 | 1.2 | 0.2 | 1.2 | 1.34E+00 | 1.0 | 0.5 | 1.0 | 2.60E-01 | 2.3 | 0.5 | 2.2 | 2.61E-01 | 1.3 | 0.1 | 1.2 |
| 1.0 | 1 | 1.39E+00 | 6.9 | -2.4 | 7.1 | 1.36E+00 | 6.2 | -0.3 | 6.4 | 2.88E-01 | 12.1 | -9.7 | 13.3 | 2.78E-01 | 10.2 | -6.0 | 11.1 | |
| | 5 | 1.35E+00 | 2.8 | 0.1 | 2.8 | 1.35E+00 | 3.1 | -0.1 | 3.0 | 2.57E-01 | 4.8 | 1.7 | 4.6 | 2.61E-01 | 5.3 | 0.2 | 5.1 | |
| | 10 | 1.36E+00 | 1.8 | -0.4 | 1.8 | 1.36E+00 | 2.0 | -0.3 | 2.0 | 2.62E-01 | 3.1 | -0.2 | 3.0 | 2.64E-01 | 3.4 | -0.8 | 3.4 | |

Table 11. As in Fig. 12, but for E_u Regression Products.

| Water Type | Depl. Speed [ms ⁻¹] | Meas. Density [in ⁻¹] | E_{u0} | | | K_{E_u} | | | LN CV | δ | σ | | | | | | |
|------------|---------------------------------|-----------------------------------|--------------|----------|----------|-----------|----------|-------|----------|----------|----------|----------|----------|----------|------|------|-----|
| | | | μ | NL CV | δ | σ | μ | NL CV | | | | δ | σ | | | | |
| Case-1 | 0.2 | 1 5 10 | 8.19E-02 | 0.0 | 0.0 | 8.19E-02 | 0.0 | 0.0 | 7.20E-03 | 1.5 | -0.4 | 1.5 | 7.20E-03 | 1.5 | -0.4 | 1.5 | |
| | | | 8.19E-02 | 0.0 | 0.0 | 8.19E-02 | 0.0 | 0.0 | 7.10E-03 | 0.8 | 0.6 | 0.7 | 7.10E-03 | 0.8 | 0.5 | 0.7 | |
| | | | 8.19E-02 | 0.0 | 0.0 | 8.19E-02 | 0.0 | 0.0 | 7.10E-03 | 0.6 | -0.1 | 0.6 | 7.20E-03 | 0.6 | -0.2 | 0.6 | |
| | 0.6 | 1 5 10 | 8.19E-02 | 0.1 | 0.0 | 8.19E-02 | 0.1 | 0.0 | 7.20E-03 | 4.2 | -0.5 | 4.6 | 7.20E-03 | 4.2 | -0.6 | 4.5 | |
| | | | 8.19E-02 | 0.0 | 0.0 | 8.19E-02 | 0.0 | 0.0 | 7.10E-03 | 2.1 | 0.7 | 2.0 | 7.10E-03 | 2.0 | 0.6 | 2.0 | |
| | | | 8.19E-02 | 0.0 | 0.0 | 8.19E-02 | 0.0 | 0.0 | 7.10E-03 | 1.8 | 0.0 | 1.7 | 7.10E-03 | 1.8 | 0.0 | 1.7 | |
| | 1.0 | 1 5 10 | 8.18E-02 | 0.1 | 0.0 | 8.18E-02 | 0.1 | 0.0 | 6.80E-03 | 8.6 | 4.1 | 8.4 | 6.80E-03 | 8.5 | 4.0 | 8.4 | |
| | | | 8.19E-02 | 0.0 | 0.0 | 8.19E-02 | 0.0 | 0.0 | 7.00E-03 | 3.3 | 1.5 | 3.2 | 7.00E-03 | 3.3 | 1.5 | 3.1 | |
| | | | 8.19E-02 | 0.1 | 0.0 | 8.19E-02 | 0.1 | 0.0 | 7.00E-03 | 4.2 | 1.5 | 3.9 | 7.00E-03 | 4.1 | 1.4 | 3.8 | |
| | NAP | 0.2 | 1 5 10 | 3.56E-02 | 0.3 | 1.0 | 3.58E-02 | 0.3 | 0.6 | 2.19E-01 | 0.6 | 2.5 | 0.6 | 2.23E-01 | 0.5 | 1.1 | 0.6 |
| | | | | 3.57E-02 | 0.2 | 0.6 | 3.60E-02 | 0.2 | 0.0 | 2.22E-01 | 0.3 | 1.2 | 0.3 | 2.27E-01 | 0.3 | -0.7 | 0.3 |
| | | | | 3.58E-02 | 0.1 | 0.6 | 3.60E-02 | 0.1 | 0.0 | 2.23E-01 | 0.2 | 1.2 | 0.3 | 2.27E-01 | 0.2 | -0.7 | 0.2 |
| 0.6 | | 1 5 10 | 3.55E-02 | 0.5 | 1.4 | 3.55E-02 | 0.5 | 1.2 | 2.13E-01 | 1.5 | 5.2 | 1.5 | 2.15E-01 | 1.4 | 4.4 | 1.3 | |
| | | | 3.58E-02 | 0.3 | 0.5 | 3.60E-02 | 0.2 | -0.1 | 2.23E-01 | 0.6 | 1.0 | 0.5 | 2.28E-01 | 0.4 | -1.0 | 0.3 | |
| | | | 3.57E-02 | 0.1 | 0.7 | 3.59E-02 | 0.1 | 0.1 | 2.22E-01 | 0.3 | 1.3 | 0.3 | 2.27E-01 | 0.2 | -0.7 | 0.2 | |
| 1.0 | | 1 5 10 | 3.59E-02 | 0.6 | 0.0 | 3.62E-02 | 0.4 | -0.8 | 2.26E-01 | 1.1 | -0.7 | 1.0 | 2.31E-01 | 0.7 | -2.9 | 0.7 | |
| | | | 3.60E-02 | 0.3 | -0.2 | 3.63E-02 | 0.3 | -0.9 | 2.28E-01 | 0.6 | -1.2 | 0.6 | 2.32E-01 | 0.4 | -3.1 | 0.4 | |
| | | | 3.60E-02 | 0.2 | -0.1 | 3.63E-02 | 0.2 | -0.7 | 2.27E-01 | 0.3 | -0.9 | 0.2 | 2.32E-01 | 0.2 | -2.8 | 0.2 | |
| CDOM | | 0.2 | 1 5 10 | 1.60E-03 | 4.1 | -1.5 | 1.70E-03 | 8.6 | -8.1 | 1.11E+00 | 5.2 | -1.1 | 5.1 | 1.17E+00 | 7.6 | -7.1 | 7.8 |
| | | | | 1.60E-03 | 1.9 | -0.6 | 1.60E-03 | 2.6 | -4.3 | 1.10E+00 | 2.1 | -0.2 | 2.1 | 1.14E+00 | 2.5 | -3.7 | 2.6 |
| | | | | 1.60E-03 | 1.8 | 0.5 | 1.60E-03 | 2.6 | -2.3 | 1.09E+00 | 1.6 | 0.5 | 1.6 | 1.13E+00 | 2.4 | -2.8 | 2.4 |
| | 0.6 | 1 5 10 | 1.50E-03 | 17.7 | 3.6 | 1.60E-03 | 13.8 | -1.1 | 1.04E+00 | 16.7 | 5.6 | 15.7 | 1.12E+00 | 11.9 | -1.7 | 11.9 | |
| | | | 1.60E-03 | 6.4 | -0.8 | 1.50E-03 | 8.5 | 5.0 | 1.12E+00 | 6.4 | -2.0 | 6.8 | 1.06E+00 | 7.4 | 3.6 | 7.3 | |
| | | | 1.60E-03 | 7.6 | -0.7 | 1.60E-03 | 7.2 | -2.6 | 1.11E+00 | 6.4 | -0.8 | 6.7 | 1.13E+00 | 5.5 | -3.1 | 5.7 | |
| | 1.0 | 1 5 10 | 1.50E-03 | 23.1 | 5.6 | 1.60E-03 | 28.1 | -2.0 | 1.08E+00 | 19.9 | 1.9 | 18.9 | 1.13E+00 | 22.8 | -2.7 | 22.7 | |
| | | | 1.50E-03 | 10.4 | 2.5 | 1.60E-03 | 16.4 | -2.1 | 1.07E+00 | 7.6 | 2.6 | 7.4 | 1.11E+00 | 11.8 | -1.3 | 12.1 | |
| | | | 1.60E-03 | 7.7 | 1.4 | 1.60E-03 | 8.2 | -3.2 | 1.07E+00 | 5.5 | 2.8 | 5.3 | 1.12E+00 | 6.4 | -2.3 | 6.7 | |

Table 12. As in Fig. 10, but for L_{00} Regression Products.

| Water Type | Depth Speed [ms ⁻¹] | Meas. Density [m ⁻¹] | L_{00} | | | K_{L0} | | | LN CV | LN δ | σ | | | | |
|------------|---------------------------------|----------------------------------|----------|----------|-------------|----------|-------|----------|----------|-------------|----------|-------------|----------|------|-----|
| | | | μ | NL CV | NL δ | σ | μ | NL CV | | | | NL δ | σ | | |
| Case-1 | 0.2 | 11 | 1 | 2.04E-02 | 0.1 | 0.0 | 0.1 | 2.04E-02 | 1.9 | 1.0 | 2.0 | 1.04E-02 | 2.0 | 1.0 | 2.0 |
| | | | 5 | 2.04E-02 | 0.1 | 0.0 | 0.1 | 2.04E-02 | 1.9 | -0.4 | 1.7 | 1.05E-02 | 1.9 | -0.5 | 1.7 |
| | | | 10 | 2.04E-02 | 0.0 | 0.0 | 0.0 | 2.04E-02 | 1.0 | -0.2 | 0.9 | 1.05E-02 | 1.0 | -0.2 | 0.9 |
| | 0.6 | 18 | 1 | 2.04E-02 | 0.1 | 0.0 | 0.1 | 2.04E-02 | 5.0 | -0.4 | 4.9 | 1.05E-02 | 5.1 | -0.4 | 5.0 |
| | | | 5 | 2.04E-02 | 0.1 | 0.0 | 0.0 | 2.04E-02 | 2.4 | 0.3 | 2.5 | 1.04E-02 | 2.4 | 0.3 | 2.5 |
| | | | 10 | 2.04E-02 | 0.0 | 0.0 | 0.0 | 2.04E-02 | 2.8 | -0.3 | 2.2 | 1.04E-02 | 2.8 | -0.3 | 2.2 |
| | 1.0 | 22 | 1 | 2.04E-02 | 0.1 | 0.0 | 0.1 | 2.04E-02 | 4.5 | 0.1 | 4.0 | 1.05E-02 | 4.6 | 0.1 | 4.0 |
| | | | 5 | 2.04E-02 | 0.1 | 0.0 | 0.0 | 2.04E-02 | 2.4 | 1.2 | 1.8 | 1.03E-02 | 2.4 | 1.2 | 1.8 |
| | | | 10 | 2.04E-02 | 0.0 | 0.0 | 0.0 | 2.04E-02 | 1.7 | -0.5 | 1.6 | 1.05E-02 | 1.7 | -0.5 | 1.6 |
| | NAP | 0.2 | 7 | 1 | 8.20E-03 | 0.5 | 0.0 | 0.5 | 8.30E-03 | 0.4 | -0.4 | 0.5 | 2.51E-01 | 0.7 | 0.3 |
| 5 | | | | 8.20E-03 | 0.2 | 0.1 | 0.2 | 8.30E-03 | 0.1 | -0.3 | 0.1 | 2.51E-01 | 0.3 | 0.4 | 0.3 |
| 10 | | | | 8.20E-03 | 0.1 | 0.1 | 0.1 | 8.30E-03 | 0.1 | -0.4 | 0.1 | 2.51E-01 | 0.2 | 0.3 | 0.2 |
| 0.6 | | 11 | 1 | 8.20E-03 | 0.2 | 0.2 | 0.2 | 8.30E-03 | 0.4 | -0.1 | 0.4 | 2.50E-01 | 0.4 | 0.5 | 0.6 |
| | | | 5 | 8.20E-03 | 0.3 | 0.1 | 0.3 | 8.30E-03 | 0.3 | -0.3 | 0.2 | 2.51E-01 | 0.4 | 0.2 | 0.4 |
| | | | 10 | 8.20E-03 | 0.3 | 0.1 | 0.2 | 8.30E-03 | 0.2 | -0.3 | 0.2 | 2.51E-01 | 0.5 | 0.4 | 0.4 |
| 1.0 | | 13 | 1 | 8.30E-03 | 0.6 | -0.2 | 0.6 | 8.30E-03 | 0.7 | -0.6 | 0.7 | 2.51E-01 | 1.2 | 0.2 | 1.2 |
| | | | 5 | 8.20E-03 | 0.4 | 0.1 | 0.4 | 8.30E-03 | 0.4 | -0.3 | 0.5 | 2.51E-01 | 0.5 | 0.3 | 0.5 |
| | | | 10 | 8.20E-03 | 0.3 | 0.2 | 0.3 | 8.30E-03 | 0.4 | -0.2 | 0.3 | 2.50E-01 | 0.5 | 0.6 | 0.5 |
| CDOM | | 0.2 | 21 | 1 | 4.00E-04 | 3.4 | 0.2 | 3.7 | 4.00E-04 | 3.4 | -1.5 | 3.7 | 1.09E+00 | 2.6 | 0.6 |
| | 5 | | | 4.00E-04 | 1.3 | 0.5 | 1.3 | 4.00E-04 | 1.2 | -0.3 | 1.2 | 1.09E+00 | 1.2 | 0.8 | 1.1 |
| | 10 | | | 4.00E-04 | 0.6 | 0.6 | 0.6 | 4.00E-04 | 0.6 | -0.1 | 0.7 | 1.09E+00 | 0.5 | 0.8 | 0.5 |
| | 0.6 | 11 | 1 | 4.00E-04 | 2.9 | -0.5 | 2.4 | 4.00E-04 | 1.6 | -0.6 | 1.7 | 1.10E+00 | 3.2 | -0.1 | 2.9 |
| | | | 5 | 4.00E-04 | 2.0 | -0.1 | 2.2 | 4.00E-04 | 2.5 | -0.6 | 2.7 | 1.10E+00 | 2.2 | 0.2 | 2.4 |
| | | | 10 | 4.00E-04 | 1.4 | 1.2 | 1.2 | 4.00E-04 | 0.8 | 0.5 | 0.8 | 1.09E+00 | 1.3 | 1.1 | 1.2 |
| | 1.0 | 9 | 1 | 4.00E-04 | 7.6 | -0.7 | 7.6 | 4.00E-04 | 6.7 | -2.5 | 7.2 | 1.10E+00 | 5.5 | 0.0 | 5.6 |
| | | | 5 | 4.00E-04 | 2.8 | 0.3 | 3.1 | 4.00E-04 | 1.9 | 0.3 | 2.2 | 1.09E+00 | 2.3 | 0.5 | 2.4 |
| | | | 10 | 4.00E-04 | 1.8 | 0.4 | 1.8 | 4.00E-04 | 1.7 | -0.2 | 1.9 | 1.09E+00 | 1.6 | 1.0 | 1.6 |

Statistical figures are indicated as follows: 1) μ is the average of the data regression products; 2) CV is the variation coefficient of μ ; 3) δ is the average of percent differences determined with Eq. 15, between the investigated regression products and the corresponding values obtained with the NL regression of full-resolution radiometric values—*i.e.*, the reference quantity in this work; and finally 4) σ is the standard deviation of the δ values. Table entries in shade of gray highlight values outside a target interval of $\pm 2\%$ for CV, δ or σ values (slightly increased with respect to that applied to discuss results in Table 8 for 24-bit simulated data).

Table 10 indicates that the CV values of E_{d0} are in most cases within 2% for a deployment speed of 0.2ms^{-1} when the multicast scheme benefits of the combination of 10 independent casts. The values of CV tend to increase at higher deployment speeds and for a lower number of casts. This further confirms the need for increasing the measurements density to enhance the precision of regression results. It is noted the similarity between values of CV and σ values, which is explained by their dependence on the closeness between the average regression products (*i.e.*, μ) and reference quantity (*i.e.*, NL full-resolution regression products).

In agreement with the analysis presented in Sec. 3.3 for an ideal instrument, the present evaluation of the multicasting scheme for hyperspectral measurements simulated for radiometers commonly used in the field, further remarks the difficulty to accurately retrieve K_{E_d} in Case-1 waters in the subsurface layer due to the low attenuation coefficient and the presence of wave perturbations. Results in Table 11 document the quality of E_u regression products. Namely, all δ and σ values for E_{u0} are within the $\pm 2\%$ uncertainty interval in Case-1 and NAP-dominated waters. A performance degradation is nevertheless observed for K_{E_u} determined in the Case-1 waters when the data density is less than 20 measurements per unit depth. The low SNR characterizing E_u in CDOM-dominated waters is again the limiting factor for an accurate determination of both E_{u0} and K_{E_u} .

Finally, Table 12 shows an overall higher accuracy of L_u results with respect to the E_d and E_u regression products discussed above. Typically, a measurement density of at least 10m^{-1} leads to values of δ and σ for L_{u0} within the $\pm 2\%$ target interval considered in this latter analysis regardless of the water type. As already noted for K_{E_d} and K_{E_u} , also the determination of K_{L_u} in Case-1 waters is subject to a decrease in performance with respect to L_{u0} . It is finally observed that the multicasting technique remains of strategic importance in CDOM-dominated waters.

5. Summary and conclusions

Ocean color applications for environmental monitoring and climate change studies rely on highly-accurate in situ validation measurements. However, the determination of field radiometric data products is sometimes based on assumptions whose validity is restricted to ideal cases. Matter of this study has been evaluating the effects of integration time on in-water radiometric data collected with hyperspectral profiling systems. The analysis has been executed simulating the radiative transfer processes with the MOX Monte Carlo code to represent realistic measurement conditions. Simulation features include the capability of discretizing the sea-surface with a resolution of 0.0012 m, and the in-water fields with 0.01 and 0.001 m horizontal and vertical resolutions, respectively.

Virtual E_d , E_u and L_u radiometric measurements were computed from the accumulation of photons over time intervals ranging from 8 to 2048 ms. Optical profiles were then constructed to evaluate subsurface radiometric values and diffuse attenuation coefficients assuming a 24-bit ADC. Both linear and non-linear regression methods have been applied to obtain data products from alternative determinations of measurement depths. The study has documented the best performance of the WGT depth definition relying on depth values weighted by the diffuse attenuation coefficient. However, close statistical figures (in most cases within 1%) have been obtained with the Avg depths relying on the mean depth within the integration interval. Instead, both the FST and LST depths (*i.e.*, corresponding to the beginning or the end, respectively, of

each integration interval) should not be adopted to avoid biased estimates of diffuse attenuation coefficients and sub-surface values, mostly for E_u and L_u data collected in waters exhibiting a high absorption coefficient.

The analysis of simulated optical profiles has provided additional manifold insights. Largely biased K_{E_d} values have been observed in Case-1 waters due to the combined effects of integration time and light focusing. A main finding is however that the integration time can partially compensate the underestimates produced by the linear fit of log-transformed data. The complementary use of both linear and non-linear schemes for the regression of optical profile measurements is then devised as a solution to evaluate the effects of light focusing and defocusing in an operational framework addressed to account for the accuracy of data products.

The study has also investigated the capability of simulating profile data obtained from HyperOCR in-water hyperspectral systems fully accounting for their features (*i.e.*, 16-bit digitization with 10-count noise, 250 ms latency time and 1 dark-signal recording after every 5 successive measurements). As expected, the decrease in the density of profile data and the lessening of SNR with respect to the ideal case (*i.e.*, 24-bit digitization with 10-count noise and negligible latency time) significantly affect the radiometric accuracy, challenging regression products in highly absorbing waters.

Overall, the study indicates that an inappropriate definition of the measurement depths likely added to an unfavorable SNR, may become a source of large uncertainties for data products determined from in-water hyperspectral profile data. It is thus essential that, in view of meeting requirements for satellite ocean color applications, the suggested WGT or alternatively the Avg schemes are applied. The analysis also indicates that an increase of the number of measurements per unit depth obtained through the multicasting technique leads to an increase of the precision of regression products, also for systems characterized by variable acquisition rates.

Finally, the work further reinforces the relevance of numerical simulations of photons transport as a mean to advance the understanding of uncertainty budgets affecting the collection of in situ radiometric data and to investigate the related measurement protocols.

Acknowledgments

The computer simulations presented in this paper were executed on the Navigator supercomputer (University of Coimbra, Portugal) through the FCT/UNL project “Large-scale parallel Monte Carlo simulations for Ocean Colour applications”. Personnel of Satlantic is duly acknowledged for the willingness to discuss technical details on the HyperOCR radiometers. The authors would also like to thank the two anonymous reviewers for their helpful comments.